

## RESEARCH ARTICLE

# Aquaporin regulates cell rounding through vacuole formation during endothelial-to-hematopoietic transition

Yuki Sato<sup>1,\*\*</sup>, Mugiho Shigematsu<sup>1,\*</sup>, Maria Shibata-Kanno<sup>1,‡</sup>, Sho Maejima<sup>2,§</sup>, Chie Tamura<sup>1</sup> and Hiroataka Sakamoto<sup>2,¶</sup>

## ABSTRACT

Endothelial-to-hematopoietic transition (EHT) is crucial for hematopoietic stem cell (HSC) generation. During EHT, the morphology of hemogenic endothelial cells (HECs) changes from flat and adherent to spherical hematopoietic cells, which detach from the dorsal aorta. HECs attain a rounded shape in a mitosis-independent manner before cell adhesion termination, suggesting an atypical cell-rounding mechanism. However, the direct mechanisms underlying this change in cell morphology during EHT remain unclear. Here, we show that large vacuoles were transiently formed in avian HECs, and that aquaporin 1 (AQP1) was localized in the vacuole and plasma membranes. Overexpression of AQP1 in non-HECs induced ectopic vacuole expansion, cell rounding and subsequent cell detachment from the endothelium into the bloodstream, mimicking EHT. Loss of redundant AQP functions by CRISPR/Cas9 gene editing in HECs impeded the morphological EHT. Our findings provide the first evidence to indicate that morphological segregation of hematopoietic cells from endothelial cells is regulated by water influx into vacuoles. These findings provide important insights for further exploration of the mechanisms underlying cell/tissue morphogenesis through water-adoptive cellular responses.

**KEY WORDS:** Endothelial-to-hematopoietic transition, Aquaporin, Vacuole, Cell rounding, Chick, Quail

## INTRODUCTION

Hematopoietic cell clusters containing hematopoietic stem cells (HSCs) arise directly from hemogenic endothelial cells (HECs) that are localized to the ventral part of the dorsal aorta (hereafter referred to as the aorta) during embryogenesis (Boisset et al., 2010; Jaffredo et al., 2000; Kissa and Herbomel, 2010; Pardanaud et al., 1996). Endothelial-to-hematopoietic transition (EHT) is a highly conserved transdifferentiation event leading to the generation of definitive HSCs in most vertebrate embryos (Dieterlen-Lièvre and Martin, 1981; Dzierzak and Bigas, 2018; Garcia-Porrero et al., 1995; Klaus and Robin, 2017). Extrinsic signaling cues and transcriptional

regulatory networks associated with HEC specification and hematopoietic cell emergence have been closely studied (Dzierzak and Bigas, 2018; Wu and Hirschi, 2021); however, the mechanisms underlying the morphological transition from flat endothelial cells to round hematopoietic cells remain unclear. Runx1 is an essential transcription factor for EHT (Chen et al., 2009; Eliades et al., 2016; Howell et al., 2021; North et al., 1999). Notably, *Runx1*-deficient mouse embryos lack vacuole-like organelles with a spherical and ultralow electron-density structure in their prospective HECs. These cells have further been noted to exhibit irregular cell flattening (North et al., 1999). This suggests the involvement of vacuoles in the process of cell rounding; however, the mechanisms underlying their generation as well as their biological roles in HECs remain unclear.

In plants, vacuoles play a pivotal role in the regulation of cell morphology and size in response to osmotic pressure. Aquaporin (AQP) family proteins mediate water transport in both cell and vacuole membranes (Maurel et al., 2015). In animal models, water influx through AQP1 promotes migration of vascular endothelial cells, cancer cells, bone marrow mesenchymal cells and neural crest cells (De Ieso and Yool, 2018; Huebert et al., 2010; Kao et al., 2017; McLennan et al., 2020; Meng et al., 2014; Saadoun et al., 2005). Overexpression of AQP1 is known to increase the invasive potential of tumor cells (Hu et al., 2006). In addition to AQP1, AQP3, AQP5 and AQP9 are known to promote epithelial-to-mesenchymal transition (EMT, Wagner et al., 2022). Furthermore, AQP expression and channel function are regulated by osmotic and hydrostatic pressure, fluid shear stress, and hypoxia (Huo et al., 2021; Kao et al., 2017; Morishita et al., 2019; Nguyen et al., 2015; Verkman, 2002). Given that HECs in the aorta directly contact blood flow, they are more likely to take up water directly in response to these mechanophysiological stimuli.

During EHT in zebrafish embryos, HECs begin rounding toward the basal side of the aorta endothelium; subsequently, hematopoietic cells are extruded into the sub-aortic space. In this process, apical membrane invagination and subsequent cavity formation through circumferential actomyosin contraction are accompanied by cell rounding (Lancino et al., 2018). In contrast, within amniote embryos, HECs begin rounding toward the apical side, and hematopoietic cells are released directly into the aortic lumen (Boisset et al., 2010). The cellular mechanisms that control morphological changes during EHT in amniote embryos have not been defined, in comparison with those in fish embryo. Avian embryos serve as an appropriate model system for hematopoietic research because they readily undergo various embryo manipulations, including tissue transplantation, exogenous gene transduction and live imaging (Asai et al., 2020; Jaffredo et al., 2010; Kulesa et al., 2013). In the current study, we sought to better understand the regulatory mechanisms underlying morphological transition from HECs to hematopoietic cells in amniotes. To this end, we characterized vacuoles in HECs using chick and quail embryo models, analyzed AQP1 localization and proposed a simple model of endothelial cell rounding by water permeation.

<sup>1</sup>Graduate School of Medical Sciences, Kyushu University, Fukuoka 812-0054, Japan. <sup>2</sup>Ushimado Marine Institute, Graduate School of Natural Science and Technology, Okayama University, Setouchi 701-4303, Okayama, Japan.

\*Present address: Japan Science and Technology Agency (JST), Kawaguchi 332-0012, Saitama, Japan; <sup>‡</sup>Present address: Daiichisankyo RD Novare, Tokyo 134-0081, Japan; <sup>§</sup>Present address: Department of Anatomy and Neurobiology, Kindai University Faculty of Medicine, Sayama 589-0014, Japan. <sup>¶</sup>Present address: Graduate School of Environmental, Life, Natural Science and Technology, Okayama University, Okayama 700-8530, Japan.

\*\*Author for correspondence (sato.yuki.299@m.kyushu-u.ac.jp)

Y.S., 0000-0001-8974-2059; M.S., 0000-0003-2357-2602; M.S.-K., 0000-0002-1773-9624; S.M., 0000-0003-1649-1716; H.S., 0000-0002-6224-4591

## RESULTS

### Vacuoles are specifically formed during EHT

In this study, we selected chick or quail embryos, depending on the availability of genetic resources, markers and live imaging (Motono et al., 2010; Pardanaud et al., 1987; Sato et al., 2010). Based on a report that untagged fluorescent proteins are excluded from vacuoles (Garcia et al., 2017), we used transgenic (tg) chick embryos, tg(pLSiΔAeGFP) (Motono et al., 2010), that express eGFP ubiquitously, to quantitatively characterize the vacuoles. Runx1-positive HECs were found in the aortic floor from embryonic day (E) 2.5 to 4 (Fig. 1A-C,E). During this period, eGFP-negative regions were observed in the HECs (Fig. 1F). Concurrent with EHT completion at E5 (Yvernogeu and Robin, 2017), Runx1-positive HECs containing eGFP-negative regions were rarely observed (Fig. 1D,F). Therefore, vacuoles in the aortic floor were identified as transient organelles that may be found in HECs. Use of tg(pLSiΔAeGFP) embryos allowed the measurement of vacuole size. HECs in the floor exhibited various vacuole sizes, which were significantly larger, on average, than those in non-HECs in the roof (Fig. 1G-I).

To visualize individual cell morphologies, the lipid membrane (Teruel et al., 1999) and cytoplasm of endothelial cells in the aorta were labeled with Lyn-mCherry and eGFP, respectively, using electroporation (Fig. 1J). This sporadic cell labeling revealed an additional eGFP-negative structure that was not fully separated from the plasma membrane. We identified this structural cavity as being distinct from the vacuole (Fig. 1K,L). Additionally, large vacuoles were observed in hemispherical and nearly spherical cells, but they were not detected in fully rounded cells (Fig. 1J,M). We predicted that the cavity was a precursor of the vacuole, as most of the cavities were found in hemispherical cells. Vacuoles generally function in autophagic digestion through fusion with lysosomes or direct transition into acidic organelles (Li and Kane, 2009). No specific localization of the lysosomal membrane marker Lamp1 or the autophagosome marker LC3B was observed in eGFP-negative areas (Fig. S1). Thus, it is likely that the eGFP-negative regions are not directly involved in autophagy.

### AQP1 is localized in the plasma and vacuole membranes

To investigate AQP1 localization in avian models, we generated anti-AQP1 antibodies (Fig. S2A). We found that AQP1 was localized to both vacuolar and plasma membranes in the endothelial cells during EHT (E2.5 to 4, Fig. 2A-D; Fig. S2B-F); its expression decreased after EHT completion (E5, Fig. 2H and Fig. S2G). AQP1 expression was observed in endothelial cells of the aorta, regardless of the dorsoventral position (Fig. 2B and Fig. S2B). Notably, endothelial cells in the intersegmental vessels (ISVs) and the nearby aortic roof express high levels of AQP1 (Fig. S3A,C). Such AQP1 expression in ISVs is maintained at E5 after AQP1 downregulation in the aorta (Fig. S3B). In the aortic floor at E3.5, Runx1-positive HECs and CD45-positive hematopoietic cells expressed AQP1 (Fig. 2E,F). Consistent with previous studies in mouse embryos (North et al., 2002), CD45 was detected late after Runx1 upregulation (E3.5, Fig. 2G). AQP1 signals also overlapped CD45 signals at the intra-aortic clusters (E3.5-E4, Fig. 2H), suggesting that AQP1 expression is maintained from HEC to hematopoietic cells during EHT. As AQP1 is expressed in a broader range of endothelial cells than Runx1 and CD45, AQP1 expression is likely to be regulated independently of Runx1 and CD45. Nevertheless, downregulation of AQP1 at E5 is temporally associated with attenuated hematopoietic activity in the aortic floor (Fig. 2I). In contrast to the luminal hematopoietic clusters,

Runx1/CD45 double-positive para-aortic foci cells did not express AQP1 (E4-E5, Fig. 2G,H). Based on the localization of AQP1 in the vacuole membrane, we hypothesize that AQP1 plays a role in the cell-rounding process of HECs by mediating water permeation into vacuoles.

### AQP1 promotes ectopic vacuole formation and cell rounding

The water permeability of AQP family proteins has been studied using cell swelling analyses of *Xenopus* oocytes by overexpressing AQP proteins in various species (Preston et al., 1992; Beitz et al., 2009). Hence, we examined the effects of overexpressing AQP1 in non-HECs. To this end, the AQP1-mRFP expression vector was electroporated into an aortic roof-specific cell lineage (Pardanaud et al., 1996). The membrane-localizing reporter mRFP-CAAX (Hancock et al., 1990) was overexpressed with eGFP to serve as the control. The mRFP-CAAX-expressing endothelial cells in the roof did not exhibit large eGFP-negative areas (Fig. 3A,B). Furthermore, Runx1 expression was not detected in these cells, suggesting that vacuole expansion was Runx1 independent. The average cross-sectional size of the vacuoles of AQP1-overexpressing cells was  $11.29 \mu\text{m}^2$ , which was larger than the average size of normal vacuoles seen in the aortic floor at E4 ( $4.56 \mu\text{m}^2$ , Fig. 1H), suggesting that AQP1 overexpression expanded vacuoles above normal levels (Fig. 3C).

To determine whether the selective water transport ability of AQP1 is responsible for vacuole expansion, an AQP1 mutant for the aromatic/arginine constriction region (ar/R), AQP1(R196H)-mRFP, was overexpressed (Beitz et al., 2009; Khan et al., 2013). AQP1(R196H)-mRFP-expressing cells formed small vacuoles (Fig. 3A,B), comparable in size with those of the control lipid membrane reporter, mRFP-CAAX-overexpressing cells (Fig. 3C), indicating that water transport into the vacuoles facilitates their expansion in endothelial cells. Quantification analysis further revealed that AQP1-mRFP-overexpressing cells were significantly rounded compared with mRFP-CAAX- and AQP1(R196H)-mRFP-overexpressing cells (Fig. 3D,E). These results indicate a simple mechanism by which water influx into the vacuole promotes cell rounding. However, large vacuoles were not observed in fully spherical cells (roundness > 0.9). In contrast, hemispherical cells (roundness 0.4–0.9) possessed large vacuoles (Fig. 3F). Indeed, the scatter plot indicated no significant linear relationship between vacuole size and cell roundness in AQP1-overexpressing cells (Fig. 3G). Thus, the vacuole expansion induced by excess AQP1 contributes to the flat-to-hemispherical transition phase. Similar to vacuoles in normal HECs, these artificially expanded vacuoles later regressed through some intrinsic degradation mechanism during the completion of ectopic cell rounding. During normal development, HECs are restricted to the aortic endothelium (Gordon-Keylock et al., 2013; Zhou et al., 2016). AQP1 overexpression also caused ectopic vacuole formation and cell rounding in the cardinal vein endothelium (Fig. 3H). This indicates that excessive AQP1 can induce EHT-like morphological changes independent of the arteriovenous properties of vascular endothelial cells. Furthermore, AQP1-overexpressing cells prospectively derived from the aortic roof were found in the bloodstream of the vitelline vessels at E4. Such circulating cells were not observed in control and AQP1(R196H)-overexpressing embryos (Movie 1).

### Ectopically rounded cells enter the circulation

To confirm whether ectopically rounded cells detach from the vascular endothelium, we performed time-lapse imaging of AQP1-overexpressing quail embryos. In most amniote embryos, during

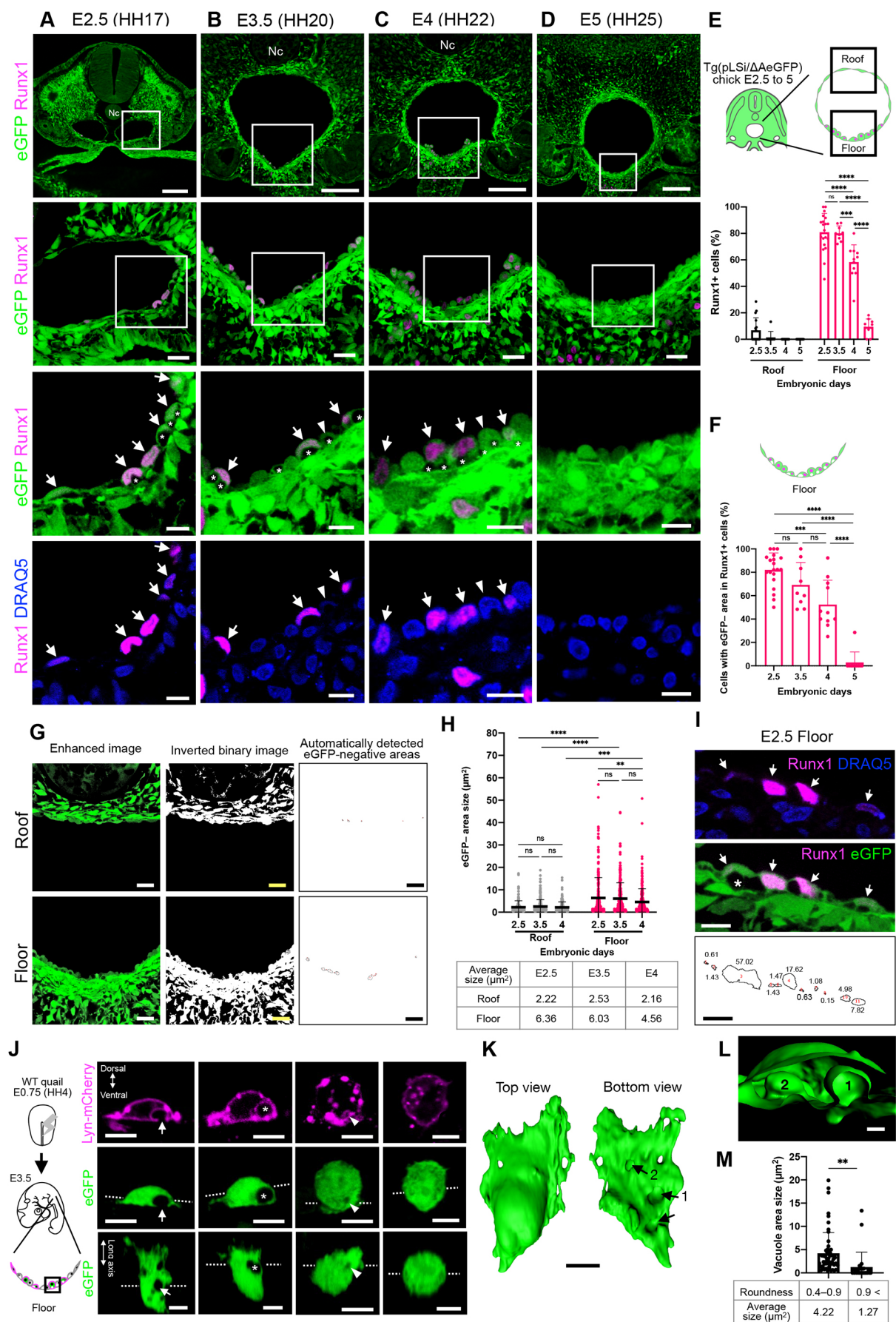




**Fig. 1. Vacuoles are transiently observed in the aorta during EHT.**

(A–D) Optical cross-sections of tg(pLSiΔAeGFP) chick embryos at E2.5 (A), E3.5 (B), E4 (C) and E5 (D). The areas shown at higher magnification are indicated by the squares. HECs were detected using anti-Runx1 immunostaining (arrows). eGFP<sup>+</sup> areas are indicated by asterisks. eGFP<sup>+</sup> part-containing cells without Runx1 expression are indicated by arrowheads. Runx1<sup>+</sup> cells underneath the aorta are hematopoietic cells stored in para-aortic foci (Fellah et al., 2013). (E) Percentage of Runx1<sup>+</sup> cells among the number of DRAQ5<sup>+</sup> nuclei in the aortic roof and floor endothelium. (F) Percentage of cells containing eGFP<sup>+</sup> parts among the Runx1<sup>+</sup> cells at each stage. (G) Inverted binary images of eGFP were used for the automatic segmentation and measurement of eGFP<sup>+</sup> areas sizes. (H) Cross-sectional area sizes of the eGFP<sup>+</sup> parts in the aortic roofs and floors at E2.5, E3.5 and E4. (I) Representative images of the eGFP<sup>+</sup> areas observed in the floor endothelium at E2.5. Outlines of the inverted images were drawn using ImageJ (bottom panel). Each number indicates eGFP<sup>+</sup> area sizes (μm<sup>2</sup>). Runx1<sup>+</sup> cells are indicated by the arrows. Extremely large eGFP<sup>+</sup> areas of over 30 μm<sup>2</sup> are cavities spanning multiple cells (asterisk). (J) Expression vectors for eGFP and Lyn-mCherry were co-electroporated into progenitor cells on the primitive streak at E0.75 (HH4). Optical cross-sections of the aortic floor (top two panels) in electroporated quail embryos at E3.5. In a hemispherical cell, an eGFP<sup>+</sup> cavity was observed on the basal side (arrows). In another hemispherical cell, eGFP<sup>+</sup> vacuoles (asterisks) delineated by a Lyn-mCherry<sup>+</sup> membrane were completely separated from the plasma membrane. A small vacuole was observed in the rounded cell (arrowheads). Bottom panels contain optically reconstructed horizontal sections. Dashed lines indicate optical slice positions. (K) Surface model of an eGFP-expressing cell. Cavities seen in the basal side are indicated by arrows. (L) Cross-section of the surface model showing internalization of eGFP<sup>+</sup> regions (arrows 1 and 2 in K). (M) Hemispherical (roundness 0.4–0.9) and fully rounded (roundness greater than 0.9) vacuole size of eGFP-labeled floor endothelial cells at E4. (E,F) E2.5, 20 slices, *n*=3; E3.5, 9 slices, *n*=3; E4, 11 slices, *n*=3; E5, 10 slices, *n*=3. (H) E2.5, 6 slices, *n*=3; E3.5, 9 slices, *n*=3; E4, 9 slices, *n*=3. (M) 81 cells, *n*=3. Error bars indicate s.d. ns, not significant; \*\**P*<0.01; \*\*\**P*<0.0005; \*\*\*\**P*<0.0001 (one-way ANOVA in E,F,H; unpaired *t*-test in M). Nc, notochord. Scale bars: 100 μm in the top panel in A; 20 μm in the second panel in A; 10 μm in the bottom two panels in A; 20 μm in G, 10 μm in I; 5 μm in J and K; 1 μm in L.

EHT stages, the aorta is located deep in the trunk, thus impeding live *in vivo* imaging analysis of EHT. Therefore, an optically accessible non-homogenic vasculature of proximal vitelline vessels at E2 (Bollerot et al., 2005) was selected for analysis (Fig. 4A). In AQP1-2A-eYFP-overexpressing embryos, eYFP-positive endothelial cells in the vitelline vessels became rounded within a few hours (Fig. 4B). The ectopically rounded cells began to flow downstream and subsequently disappeared from the image field (Movie 2). Hence, non-HEC rounding caused by excess AQP1 expression was accompanied by ectopic cell detachment from the endothelium. Moreover, in the magnified views, the eGFP-labeled control cells displayed an elongated shape with continuous migratory activity and no detectable vacuoles. In contrast, the AQP1-2A-eYFP-overexpressing cells displayed vacuoles that became undetectable as cell rounding progressed (Fig. 4C and Movie 3). Cell rounding is known to occur during mitotic cell division (Champion et al., 2017). We confirmed that no eGFP-negative regions were observed in dividing cells, suggesting that vacuoles are not involved in mitotic cell rounding in vascular endothelial cells (Movie 4).

Time-lapse imaging revealed that the ectopically rounded cells eventually disappeared from the vitelline vessels. At this stage, the number of apoptotic cells had not increased in the AQP1-2A-eYFP-overexpressing regions (Fig. S4A,B), and no abnormal nuclear morphology or DNA punctum was observed in the largely vacuolated cells (Fig. S4C). Therefore, detachment of the AQP1-overexpressing cells was not associated with apoptotic cell extrusion, and artificially formed vacuoles were not cytotoxic.

Such ectopic vacuole formation induced by AQP1 overexpression was not observed in the surrounding mesenchymal cells outside the vitelline vessels (Fig. S4D). This result suggests that AQP1-mediated vacuole formation occurs only in endothelial cells. Overexpression of AQP1 has been shown to promote lamellipodia formation in cultured epithelial cells and filopodia formation in neural crest cells (McLennan et al., 2020; Saadoun et al., 2005). In vitelline vessels, eGFP-labeled control endothelial cells exhibited filopodia with F-actin stress fibers. In contrast, endothelial cells overexpressing AQP1 did not form protrusions and showed no significant polarized accumulation of F-actin (Fig. 4D,E). This result indicates that, in endothelial cells, excess AQP1 promotes vacuole formation rather than pseudopodia formation.

In mouse and chick embryos, circulating hematopoietic cells are CD45 positive (Iizuka et al., 2016; Yvernogeu and Robin, 2017). Normally, CD45-positive cells are rarely detected in the vitelline vessels of E2 embryos (Fig. 4F). Similarly, in the AQP1-2A-eYFP-overexpressed embryo at E2, eYFP-positive endothelial cells that are ectopically rounded with vacuoles are not CD45 positive (Fig. 4G). These AQP1-2A-eYFP-overexpressing cells continued to circulate and were observed in the bloodstream at a later stage (Fig. 4H,I, Movie 5). Thus, vacuole formation induced by excess AQP1 promotes endothelial cell rounding and subsequent detachment from the vascular endothelium. In the embryo at E3, circulating CD45-positive cells normally derived from the aortic floor are found in the vitelline vessels (Fig. 4J). Furthermore, AQP1-2A-eYFP-overexpressing cells were detected as CD45-positive cells, suggesting the possibility that ectopically detached cells may have acquired hematopoietic potential during circulation (Fig. 4K,L).

**Hemogenic endothelial cells form vacuoles *in vitro***

*In vitro* reconstitution of EHT is possible in avian embryos (Yvernogeu et al., 2016). To investigate whether vacuoles and cavities are formed *in vitro*, we cultured quail embryo-derived presomitic mesoderm (PSM, Fig. 5A). Within 3 days, the QH1-positive endothelial cells were rounded and expressed AQP1 (Fig. 5B). Culture of the tg(pLSiΔAeGFP) embryo-derived PSM revealed that Runx1-positive HECs formed cavities and vacuoles (Fig. 5C,D). Additionally, AQP1 was localized in the plasma and vacuole/cavity membranes, similar to observations made *in vivo* HECs (Fig. 5E). To quantitatively compare vacuoles formed *in vivo* and *in vitro*, progenitors for the aortic floor and PSM were sporadically labeled with eGFP using electroporation (Fig. 5F). This allows automatic segmentation of both vacuoles and cell outlines. Various sizes of vacuoles were observed under *in vitro* as well as *in vivo* conditions (Fig. 5G). There were no significant differences in vacuole size and roundness between them (Fig. 5H,I). These results suggest that vacuoles are formed concurrently with EHT under *in vitro* conditions.

To characterize AQP1-expressing endothelial cells, AQP1/QH1 double-positive cells and AQP1/QH1 double-negative cells were sorted from cultured tissues and subjected to RNA-seq analysis (Fig. 5J). Differentially expressed gene (DEG) analysis of these two different cell populations revealed that genes involved in the specification of HECs and hematopoietic cells were upregulated in AQP1/QH1 double-positive cells (Fig. 5K). When the identified DEGs were classified by molecular function using gene ontology (GO) terms, there were characteristic differences in the ratios of receptors (GO: 0038023) and transcriptional regulators (GO: 0140110) in the up- and downregulated groups, respectively. In contrast, there was no significant difference in the ratio of





transmembrane transporters (GO: 0022857) (Fig. 5L). In this population, proteins encoded by *TRPM1*, *TRPC6* and *PIEZO2* that mediated mechanical stimulus (GO: 0009612), and those encoded by *SLC4A11*, *KCNMA1* and *LRRC8A* that mediated the response to

5

**Fig. 2. AQP1 is localized in the plasma and vacuole membranes of endothelial cells in the floor of the aorta.** (A-C) Optical cross-sections of a tg(pLSiΔeGFP) chick embryo at E3.5. (B) Magnified views of the areas outlined in A. (C) Magnified views of areas outlined in B. Endothelial cells in the aortic floor show eGFP<sup>+</sup> areas (asterisks). AQP1 is localized in the plasma membrane (PM) and boundaries of the eGFP<sup>+</sup> and eGFP<sup>-</sup> areas (arrowheads). (D) Immunoelectron microscopy of wild-type quail embryos at E3.5. Endothelial cells in the aortic floor contain large vacuoles (asterisks). A magnified view of the area outlined is shown in the right panel. AQP1 (6 nm gold particles) was localized in the plasma and vacuole membrane (VM). (E,F) Optical cross-sections of the aortic floor in wild-type quail embryos at E3.5. (E) AQP1 is localized in the plasma and vacuole membranes in Runx1<sup>+</sup> (arrows) and Runx1<sup>-</sup> (arrowheads) cells. (F) AQP1<sup>+</sup> cells partially overlap CD45<sup>+</sup> cells (arrows in F). (G,H) Optical cross-sections of wild-type chick embryos at E2.5, E3.5, E4 and E5. (G) Runx1<sup>+</sup>/CD45<sup>+</sup> cells in the intra-aortic cluster and para-aortic foci are indicated by arrows and arrowheads, respectively. (H) Intra-aortic cluster cells are AQP1<sup>+</sup>/CD45<sup>+</sup> (arrows), and CD45<sup>+</sup> para-aortic foci cells are negative for AQP1 (arrowheads). (I) Schematic representation of the spatiotemporal relationships of AQP1<sup>+</sup>, Runx1<sup>+</sup> and CD45<sup>+</sup> cell populations in the aortic floor during EHT. Scale bars: 50  $\mu$ m in A; 20  $\mu$ m in B,E-H; 5  $\mu$ m in C; 2  $\mu$ m in D (left); 100 nm in D (right).

(Törnroth-Horsefield et al., 2022), was included in the group with reduced expression. Although AQP1 is involved in the promotion of ECM degradation in tumor and neural crest cells (McLennan et al., 2020; Wei and Dong, 2015), no matrix metalloproteinase genes were significantly upregulated in the AQP1/QH1 double-positive cells. A major group of genes involved in EMT (GO: 000183) is also not upregulated. Based on the enriched GO terms, the AQP1/QH1 double-positive cell population was characterized as vascular endothelial cells that potentially differentiated into hematopoietic cell lineages. In contrast, genes involved in muscle formation and sensory nervous system development were suppressed (Fig. 5M).

### AQP channels are redundantly required for HEC rounding

Abnormalities in EHT have not been reported in AQP1-deficient mouse embryos (Hua et al., 2019). Therefore, to assess the requirement of AQP1 for EHT in quail embryos, we used CRISPR/Cas9 genome editing for *AQP1* knockout. AQP1-deficient endothelial cells – confirmed by loss of AQP1 protein expression – showed large vacuoles and rounded cell shapes (Fig. S5). We hypothesized that

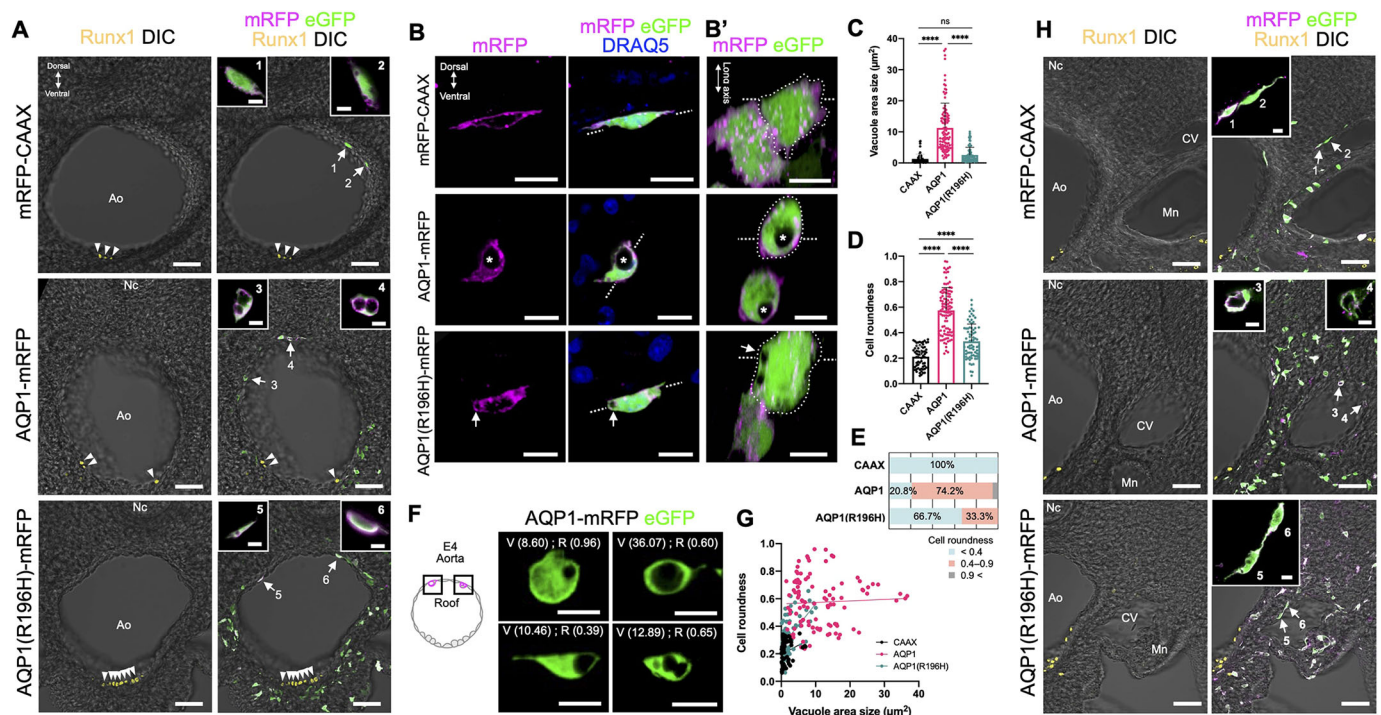


**Fig. 3. AQP1 overexpression leads to ectopic vacuole expansion and cell rounding.** (A,H) Optical cross-sections of mCherry-CAAX (control)-, AQP1-mRFP- and AQP1(R196H)-mRFP-overexpressing quail embryos at E4. eGFP was co-expressed for vacuole measurements. (A) Runx1<sup>+</sup> HECs are indicated by arrowheads. AQP1-mRFP-overexpressing endothelial cells ectopically formed large vacuoles without Runx1 expression in the roof of the aorta (arrows 3 and 4 in the middle panel). Large vacuoles were not observed in AQP1(R196H)-mRFP-overexpressing endothelial cells (arrows 5 and 6 in the bottom panel). (B,B') Representative optical cross-sections (B) and horizontal sections (B') of mCherry-CAAX-, AQP1-mRFP- and AQP1(R196H)-mRFP-overexpressing cells in the roof. Thick dashed lines indicate optical slice positions. A large vacuole was formed ectopically in AQP1-mRFP-overexpressing cells (asterisks in the middle panel). In AQP1(R196H)-mRFP-overexpressing cells, vacuoles were smaller than those in AQP1-mRFP-overexpressing cells (arrows in the bottom panels). (C) Sizes of the cross-sectional areas of vacuoles in the roof. AQP1-mRFP-overexpressing cells formed significantly larger vacuoles. (D) Roundness of vacuolated cell cross-sections. AQP1-mRFP-overexpressing cells were rounded compared with mRFP-CAAX- and AQP1(R196H)-mRFP-overexpressing cells. (E) Proportion of flat (roundness <0.4), hemispherical (roundness 0.4–0.9) and spherical (roundness >0.9) cells in each experiment. (F) Representative images of co-electroporated eGFP in AQP1-mRFP-overexpressing cells in the roof. Values in brackets are the vacuole size (V) and cell roundness (R). (G) Scatter plot of vacuole size and cell roundness shown in C and D. AQP1-mRFP-overexpressing cells were characterized by large vacuoles and increased roundness. The correlation coefficients were  $r=0.2466$  ( $P=0.0459$ ) for mRFP-CAAX,  $r=0.04878$  ( $P=0.6229$ ) for AQP1-mRFP and  $r=0.5672$  ( $P<0.0001$ ) for AQP1(R196H)-mRFP. (C–E,G) mRFP-CAAX, 66 cells,  $n=9$ ; AQP1-mRFP, 104 cells,  $n=9$ ; AQP1(R196H)-mRFP, 75 cells,  $n=9$ . Error bars indicate s.d. ns, not significant; \*\*\*\* $P<0.0001$  (one-way ANOVA). (H) AQP1-mRFP-overexpressing endothelial cells ectopically formed large vacuoles and exhibited rounded cell morphology in the cardinal vein (arrows 3 and 4 in the middle panel). Nc, notochord; Ao, aorta; CV, cardinal vein; Mn, mesonephros. Scale bars: 50  $\mu$ m in A and H; 10  $\mu$ m in B; 5  $\mu$ m in F.



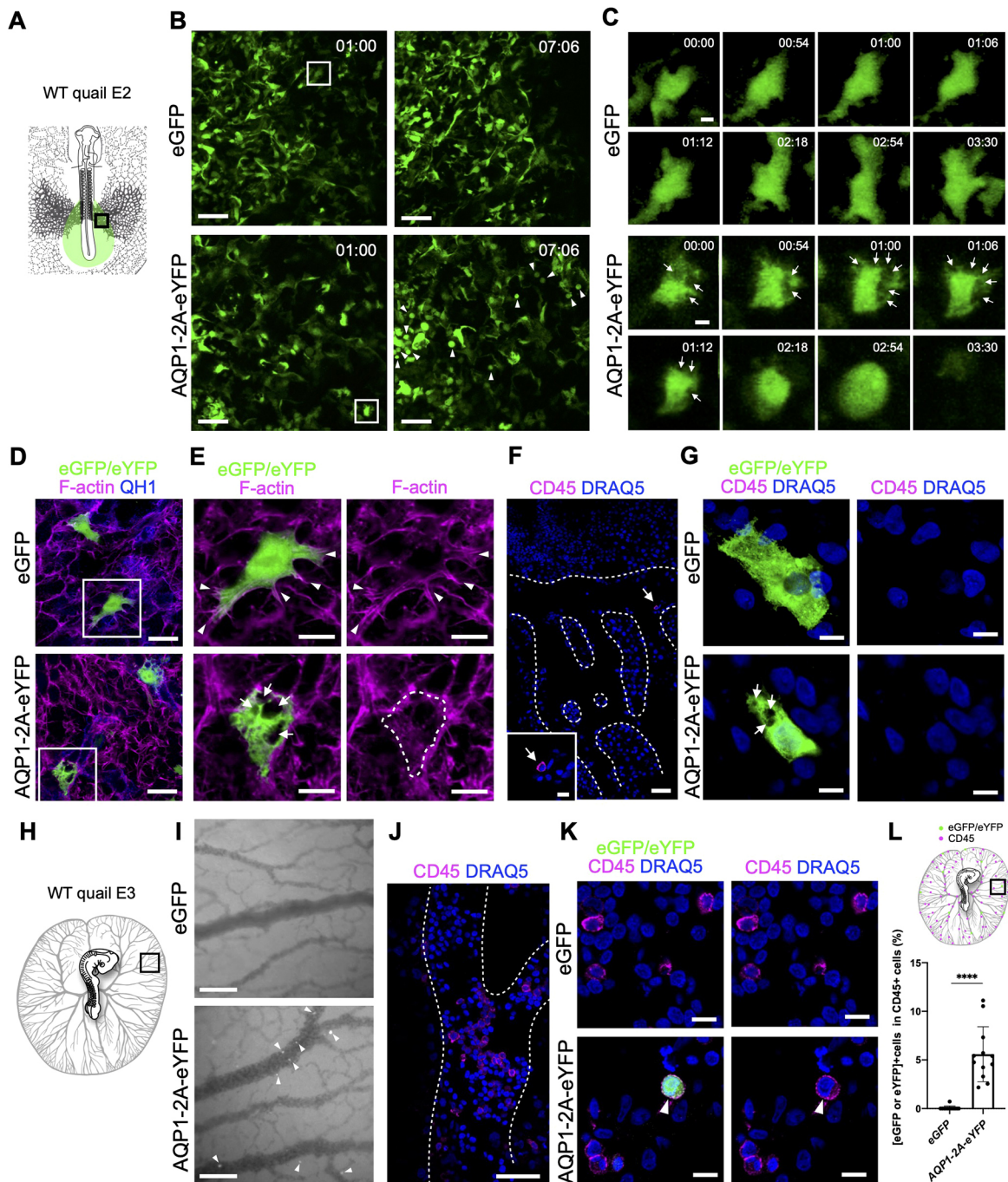


**Fig. 4. AQP1-mediated ectopic vacuole formation is accompanied by cell detachment.** (A) Illustration of an embryo 24 h after electroporation (E2, HH12) showing the electroporated region (green). Square indicates the imaged area. (B) Time-lapse observation of vitelline vessels in eGFP (control)- and AQP1-2A-eYFP-overexpressing quail embryos. AQP1-2A-eYFP-overexpressing endothelial cells became rounded and detached from vitelline vessels (arrowheads in lower panel, see Movie 2). Areas indicated in the left panels are shown at higher magnification in C. (C) Control (eGFP) cells did not form detectable vacuoles. In AQP1-2A-eYFP-overexpressing cells, vacuoles (arrows) formed concurrently with cell rounding. Eventually, AQP1-2A-eYFP-overexpressing cells were detached (see Movie 3). (D) Vitelline vessels stained with the vascular endothelial cell membrane marker QH1 and a F-actin indicator, phalloidin, 28 h after electroporation (E2, HH13). Areas indicated in are shown at higher magnification in E. (E) In control embryos, eGFP<sup>+</sup> endothelial cells showed F-actin-rich processes (arrowheads in top panels). AQP1-2A-eYFP-overexpressing endothelial cells do not form obvious protrusions and F-actin is uniformly distributed in the cytoplasm, except in vacuoles (arrows in bottom panel). (F) CD45<sup>+</sup> hematopoietic cells are sparse in E2 (HH13) embryos (arrows). The inset shows a CD45<sup>+</sup> cell found in the vitelline vessel. (G) Hemispherical AQP1-2A-eYFP-overexpressing cells with vacuoles (arrows) budding from the endothelium are not positive for CD45. (H) Illustration of a quail embryo 52 h after electroporation (E3, HH18). The area imaged in I is outlined. (I) Snapshots of peripheral vitelline artery regions in eGFP- and AQP1-2A-eYFP-electroporated embryos. The AQP1-overexpressing cells circulated through blood vessels (arrowheads in bottom panel, see Movie 5). (J) CD45<sup>+</sup> cells are found in vitelline vessels at E3. (K) eYFP<sup>+</sup>/CD45<sup>+</sup> cells are found in a vitelline vessel of an AQP1-2A-eYFP-overexpressed embryo at E3 (arrowhead in bottom panels). (L) Percentages of eGFP<sup>+</sup> or eYFP<sup>+</sup> cells among CD45<sup>+</sup> cells in the vitelline vessels of control and AQP1-2A-eYFP-overexpressed embryos (12 areas,  $n=3$  each). \*\*\*\* $P<0.0001$  (unpaired  $t$ -test). Optical horizontal sections are shown in B-G, J, K. Dashed lines indicate outlines of a cell (E) and the vitelline vessels (F and J). Scale bars: 50  $\mu$ m in B, F, J; 5  $\mu$ m in C; 20  $\mu$ m in D; 10  $\mu$ m in F (inset), G, K; 200  $\mu$ m in I.



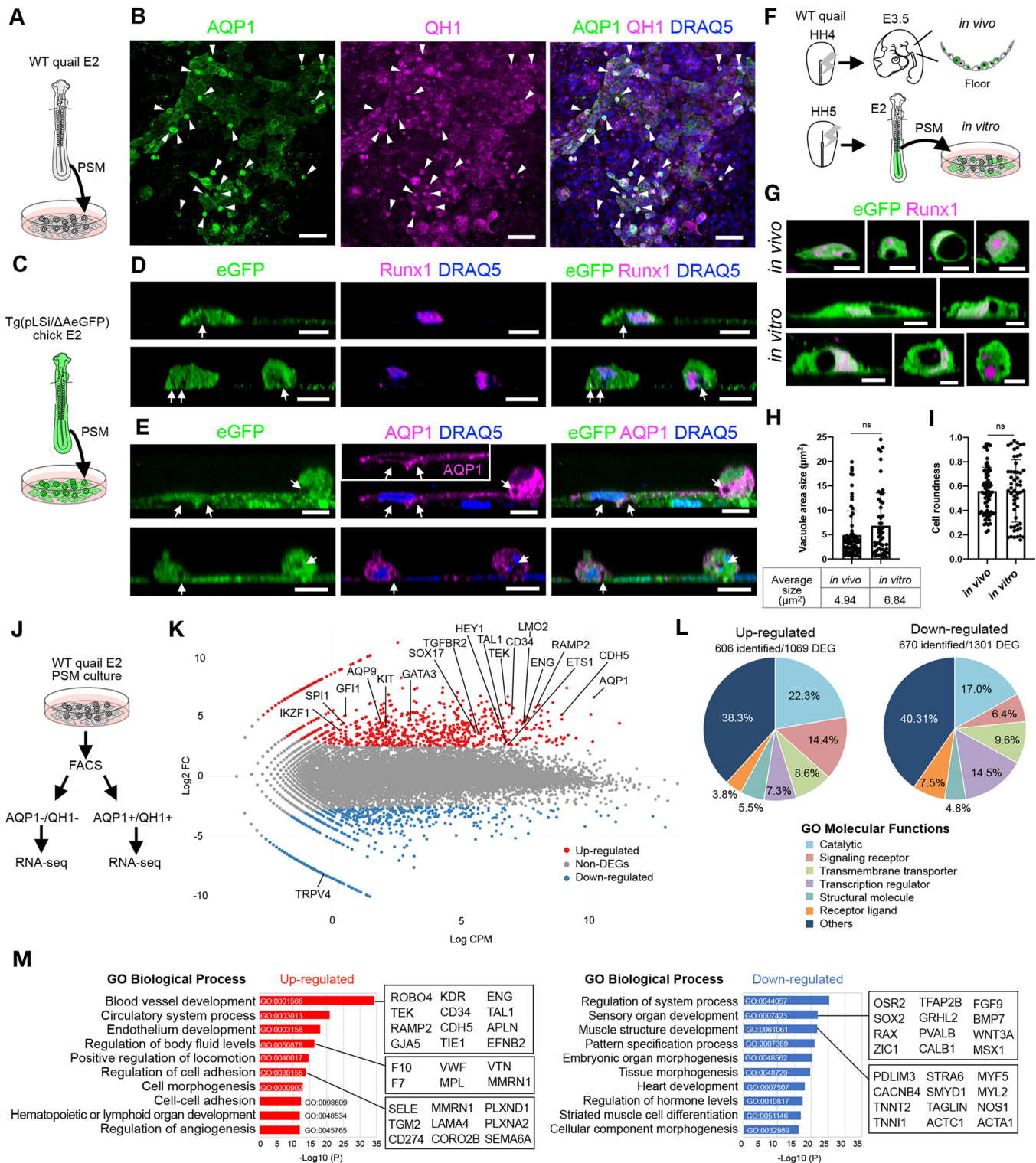


**Fig. 5. *In vitro* EHT recapitulates AQP1 localization in vacuoles/cavities.** (A) EHT in cultures of the presomitic mesoderm (PSM) isolated from quail embryos (Yvernogeu et al., 2016). (B) Z-stacked frontal images of cultured tissues at 72 h. AQP1 is expressed in QH1<sup>+</sup> endothelial cells. Rounded cells are indicated by arrowheads. (C) Tg(pLSiΔAeGFP)-derived PSM culture for vacuole/cavity detection. (D,E) Reconstructed optical cross-sections of Tg(pLSiΔAeGFP)-derived tissues at 72 h. eGFP-negative vacuoles and cavities (arrows) formed in Runx1<sup>+</sup> HECs (D). AQP1 localization in the plasma and vacuole/cavity membranes (arrows, E). (F) Sporadic eGFP-labeling of the aortic floor (for *in vivo*) and PSM cells (for *in vitro*) by electroporation. (G) Optical cross-sections of eGFP/Runx1<sup>+</sup> cells *in vivo* and *in vitro* are used for measurement. (H,I) No statistically significant difference in either vacuole size (H) or cell roundness (I) between *in vivo* and *in vitro* experiments. (J) RNA-seq for AQP1<sup>+</sup>/QH1<sup>+</sup> and AQP1<sup>-</sup>/QH1<sup>-</sup> cells at 72 h. (K) MA plot of differentially expressed genes (DEGs) in AQP1<sup>+</sup>/QH1<sup>+</sup> populations compared with AQP1<sup>-</sup>/QH1<sup>-</sup> populations. x and y axes are Log CPM (count per million) and Log<sub>2</sub> FC (fold change), respectively. Log<sub>2</sub> FC > 1, P < 0.05 and Log<sub>2</sub> FC < -1, P < 0.05 are indicated by red and blue, respectively. Hematopoiesis-related genes AQP1 and TRPV4 are indicated. (L) Functionally identified DEG ratios by gene ontology (GO) terms. (M) Top 10 enriched GO terms in AQP1<sup>+</sup> endothelial cells *in vitro*. Some of the detected genes are listed in the boxes. Scale bars: 50 μm in B; 10 μm in D,E; 5 μm in G.

AQP1 is not solely involved in EHT, as *AQP5*, *AQP8* and *AQP9* were also expressed in the endothelium of the aorta (Fig. S6A). As *AQP9* was upregulated in *AQP1*-expressing endothelial cells *in vitro* (Fig. 5G), double knockout analyses were performed; however, co-electroporation of *AQP1* and *AQP9* guide RNA (gRNA) with Cas9-2A-mRFP in HECs did not cause obvious deficiency in vacuole formation or cell rounding. Similarly, double-knockouts of *AQP1* and *AQP5*, as well as *AQP1* and *AQP8* did not induce any morphological abnormalities (Fig. S6B,C).

CRISPR/Cas9 genome editing via electroporation cannot attain 100% efficiency (Williams et al., 2018). We therefore aimed to achieve the stochastic reduction of functional AQPs in HECs by introducing multiple gRNAs for *AQP1*, *AQP5*, *AQP8* and *AQP9* with Cas9-2A-mRFP. In electroporated embryos, multiple AQP-knockout HECs (mRFP<sup>+</sup>/Runx1<sup>+</sup>) exhibited a flat morphology (Fig. 6A,B). In these embryos, the percentage of vacuolated HECs significantly decreased (Fig. 6C). Among the vacuolated cell population, notable reductions in vacuole area size and cell roundness were observed (Fig. 6D-F). Accordingly, non-vacuolated cells exhibited lower cell roundness (Fig. 6D,F). On the basal side of the multiple AQP-knockout cells, no obvious cavities were formed (Fig. 6G,H). These results indicate that concomitant AQP activities are required for vacuole/cavity formation and cell rounding. In contrast, *Runx1*-knockout endothelial cells formed vacuoles/cavities and exhibited spherical morphology (Fig. S7), suggesting that *Runx1* may not be essential for cell morphological changes during EHT in avian embryos.

As we noted previously (Figs 1 and 2), EHT was completed by E5 and *Runx1*-positive HECs disappeared from the aorta. Consistently, in control gRNA-electroporated embryos, *Runx1*-positive HECs were not found in the aorta at E5. In contrast, multiple AQP-knockout HECs were detected at this stage (Fig. 6I). Contribution of the multiple AQP-knockout HECs to the para-aortic foci was observed (Fig. 6J), indicating that only the EHT toward the aortic lumen side was affected. Tg(tie1:H2B-eYFP) quail embryos fluorescently label endothelial cells and HECs, allowing the accurate segmentation of individual cell nuclei and subsequent automatic cell counting (Sato et al., 2010). Quantification of the mRFP<sup>+</sup>/Runx1<sup>+</sup> cells in tg(tie1:H2B-eYFP) embryos revealed that multiple AQP-knockout HECs were selectively retained in the aortic floor at E5 (Fig. 6K; Fig. S8), indicating that the detachment of HECs from the endothelium was suppressed by multiple AQP knockouts. CRISPR/Cas9 genome editing via electroporation is not 100% efficient; therefore, mRFP<sup>+</sup> cells are not necessarily multiple AQP-knockout cells. In this analysis, individual cell detection was performed automatically using *Runx1* and eYFP signals in the nuclei regardless of cell shapes represented by mRFP. A population of mRFP<sup>+</sup>/Runx1<sup>+</sup> cells in which multiple AQP knockout did not occur may have been detached from the vessel wall between E4 and E5. Therefore, the percentage of mRFP<sup>+</sup>/Runx1<sup>+</sup> cells decreased at E5 compared with E4. From these results, we conclude that cell rounding and detachment during EHT are regulated by AQP-mediated water permeation into vacuoles (Fig. 6L). As it has been suggested that *AQP1* transitions from a high water-permeability state to a closed state in response to an increase in membrane tension without osmotic changes (Ozu et al., 2013), AQPs in rounded HECs may automatically stop water transport and prevent plasma membrane rupture.

## DISCUSSION

Our results suggest that vacuole expansion, cell rounding and detachment of endothelial cells by AQP are *Runx1*-independent

processes (Figs 3, 6; Fig. S7). A previous genome-wide search for *Runx1*-binding sequences in cultured mouse HECs implied that AQP genes are not involved in direct transcriptional targets of *Runx1* (Lie-A-Ling et al., 2014). However, in *Runx1* knockout mouse embryos, endothelial cells in the aortic floor lack vacuole-like structures (North et al., 1999), suggesting that *Runx1* is involved in vacuole formation. Furthermore, *Runx1* expression correlates with the progression of cell rounding in mouse embryos (Bos et al., 2015). *Runx1* also regulates the expression of genes involved in cytoskeletal reorganization (Lie-A-Ling et al., 2014). In quail embryos, the rounded morphology of *Runx1*-knockout cells (Fig. S7) was not consistent with the relatively flat cells observed in the *Runx1*-knockout mouse embryo (North et al., 1999). This suggests that the *Runx1* function for the EHT in avian embryos may be different from that in mice. In zebrafish, Gata2-mediated restoration of HSCs occurs in *Runx1*-knockout lines, suggesting a *Runx1*-independent pathway of hematopoiesis (Bresciani et al., 2021). The present loss-of-function experiment of *Runx1* in quail embryos is the first and only preliminary analysis of *Runx1* function in the avian species. More-detailed analyses in avian embryos are needed to uncover *Runx1*-independent cell rounding mechanisms during EHT.

Osmotic and hydrostatic pressure are involved in the opening/closing of the AQP channel (Nguyen et al., 2015; Verkman, 2002). Nonetheless, the mechanophysiological conditions and molecules involved in the regulation of AQP functions in HECs remain to be elucidated. We demonstrated that excess *AQP1* expression induces ectopic EHT-like cellular responses without experimental changes in osmotic and hydrostatic pressures (Figs 3 and 4). AQP proteins are assembled into a homotetramer in the plasma membrane to form the functional channel unit (Mathai and Agre, 1999). We believe that *AQP1* overexpression increases their tetramerization rate, resulting in an increased number of functional channel units, which leads to excessive vacuole enlargement in non-HECs. Although single *AQP1*-knockout HECs retained their vacuole-formation and cell-rounding abilities, multiple knockouts of redundantly expressing *AQP1*, *AQP5*, *AQP8* and *AQP9* genes in HECs led to failure of morphological EHT (Fig. 6 and Fig. S8). These results indicate that the process of endothelial cell rounding is dependent on the number of AQP channels. In this study, we have analyzed the morphological phenotypes induced by the overexpression of *AQP1*, but it has not yet been verified whether *AQP5*, *AQP8* and *AQP9* can also induce similar changes on endothelial cells when overexpressed alone. This should be investigated in detail in the future.

In the *AQP1*-expressing endothelial cells *in vitro*, a considerable number of ion channels and transporters, which may contribute to osmoregulation and/or mechano-transduction, were upregulated (Fig. 5). We, therefore, searched for deletion phenotypes of these genes; however, none of them was found to influence embryonic hematopoiesis. Generally, ion channels and transporters belong to a large family of genes with overlapping functions. Hence, the mechanophysiological activation mechanisms of AQPs require further investigation in light of the functional redundancy of these solute channels/transporters, which may have been acquired to tightly regulate EHT.

*AQP1* expression in the aorta is attenuated at the time of EHT termination. In contrast, expression in the ISV is maintained (Figs S2 and S3). As *AQP1* expression is not restricted to the aortic floor, we believe that the release of HECs into the circulation does not cause a concomitant loss of *AQP1* expression throughout the aorta from E4 to E5. There may be a regulatory mechanism of *AQP1*



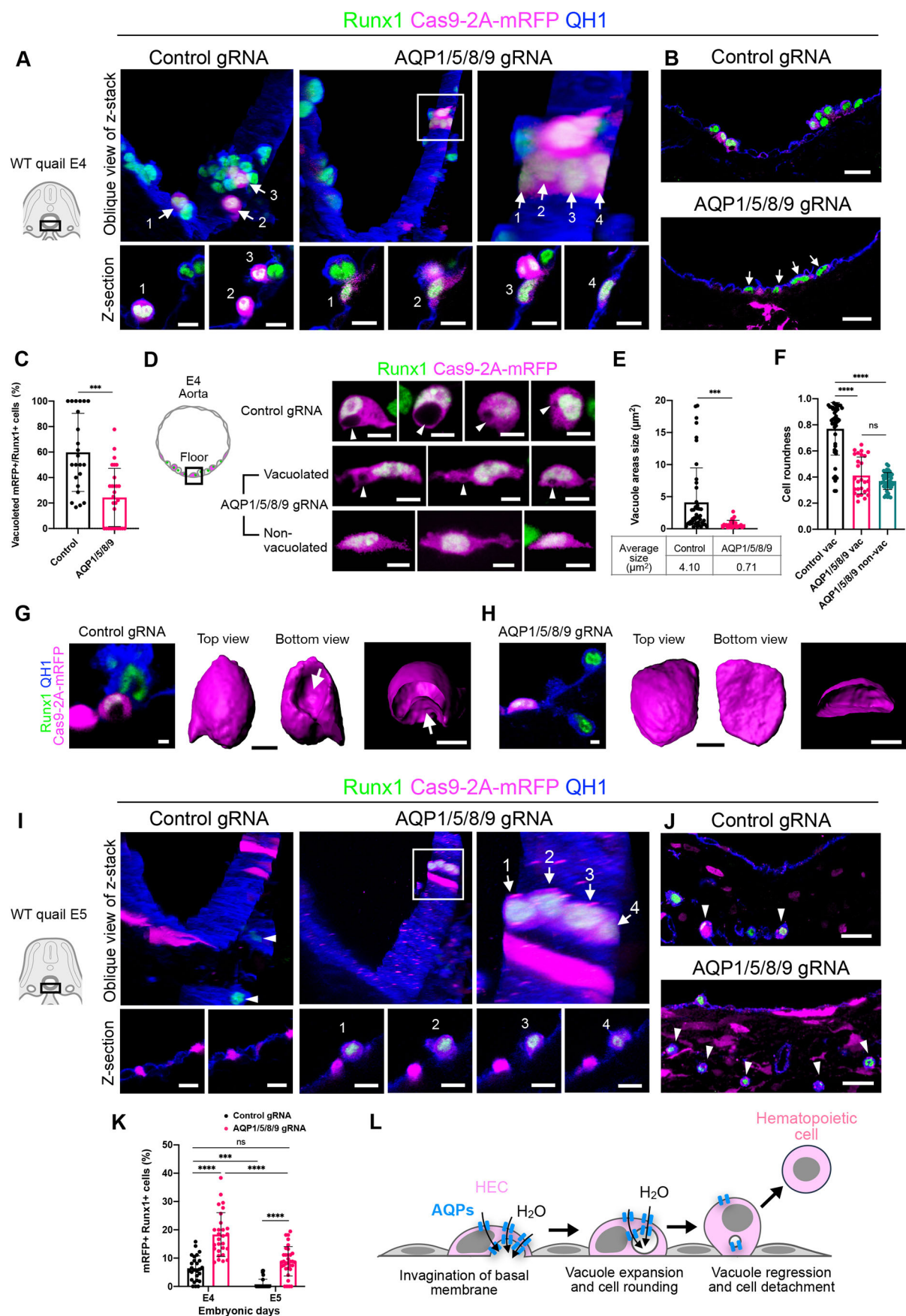


Fig. 6. See next page for legend.



**Fig. 6. Redundant AQP function is required for hemogenic endothelial cell rounding and detachment.** (A) Oblique views of z-stacked images of the aortic floor at E4 (top panels). Electroporated cell bodies and internal vacuoles were identified by mRFP. Endothelial cell membrane is detected by QH1. Arrows in the left panel indicate mRFP<sup>+</sup>/Runx1<sup>+</sup> cells in control gRNA-electroporated embryos. Arrows in the right panel indicate mRFP<sup>+</sup>/Runx1<sup>+</sup> cells in AQP1/5/8/9 gRNA-electroporated embryos. Lower panels indicate optical cross-sections of each mRFP<sup>+</sup>/Runx1<sup>+</sup> cell. (B) Optical cross-sections of the aortic floor at E4. Upper panels: mRFP<sup>+</sup>/Runx1<sup>+</sup> cells in control embryos. Lower panels: mRFP<sup>+</sup>/Runx1<sup>+</sup> cells in AQP1/5/8/9 gRNA-electroporated embryos. Arrows indicate mRFP<sup>+</sup>/Runx1<sup>+</sup> flat cells. mRFP<sup>+</sup> cells under the aorta are lateral plate-derived mesenchyme. (C) Percentage of vacuolated mRFP<sup>+</sup>/Runx1<sup>+</sup> cells among the total Runx1<sup>+</sup> cells in the control (23 slices,  $n=13$ ) and AQP1/5/8/9 gRNA-electroporated embryos (28 slices,  $n=14$ ) at E4. (D) Magnified views of representative electroporated HECs (mRFP<sup>+</sup>/Runx1<sup>+</sup>). Vacuoles are indicated by arrowheads. (E) Cross-sectional area sizes of the vacuoles in control embryos (46 cells,  $n=13$ ) and AQP1/5/8/9 gRNA-electroporated embryos (27 cells,  $n=14$ ) at E4. (F) Cell roundness of mRFP<sup>+</sup>/Runx1<sup>+</sup> cells in control embryos (46 cells,  $n=13$ ) and AQP1/5/8/9 gRNA-electroporated embryos at E4 (27 vacuolated and 46 non-vacuolated cells,  $n=14$ ). (G,H) Surface model of control cells (G) and AQP1/5/8/9 gRNA-electroporated cells (H). Cavities seen in the basal side are indicated by arrows. Cross-sections of the surface models (right panels) showing internalization of mRFP<sup>+</sup> regions (arrow in G). No cavities are observed in H. (I) Oblique views of z-stacked images of the aortic floor at E5 (upper panels). Left: mRFP<sup>+</sup>/Runx1<sup>+</sup> cells in control embryos. Arrowheads indicate Runx1<sup>+</sup> cells. Right: Arrows indicate mRFP<sup>+</sup>/Runx1<sup>+</sup> cells in AQP1/5/8/9 gRNA-electroporated embryos. Lower panels: Optical cross-sections of each mRFP<sup>+</sup>/Runx1<sup>+</sup> cell. (J) Optical cross-sections at E5. mRFP<sup>+</sup>/Runx1<sup>+</sup> para-aortic foci cells are indicated by arrowheads. (K) Percentages of mRFP<sup>+</sup>/Runx1<sup>+</sup> cells among eYFP<sup>+</sup> endothelial cells in the aortic floors of control gRNA (26 slices,  $n=5$  at E4; 30 slices,  $n=5$  at E5) and AQP1/5/8/9 gRNA (28 slices,  $n=6$  at E4; 33 slices,  $n=9$  at E5) electroporated tg(tie1:H2B-eYFP) embryos (refer to Fig. S8). (L) Model depicting HEC rounding. Error bars indicate s.d. ns, not significant, \*\*\* $P<0.001$ , \*\*\*\* $P<0.0001$ , (unpaired  $t$ -test in C,E and one-way ANOVA in F,K. Scale bars: 10  $\mu$ m in bottom panels in A and I; 20  $\mu$ m in B and H (left panel); 5  $\mu$ m in D,G,H.

expression in endothelial cells that is likely to differ from site to site; accordingly, vascular water permeability may change dynamically. Two types of water transport pathways in multicellular organisms are documented: paracellular and transcellular. Although there are not many examples, a cavity-like structure spanning two adjacent cells has been observed, especially during the early phase of EHT at E2.5 (Fig. 1). This suggests that paracellular water transport may occur in HECs. In contrast, overexpression of AQP1 resulted in autonomous vacuole formation only in transfected cells (Figs 3 and 4). Based on these experimental results, we proposed a model of AQP-mediated transcellular water transport (Fig. 6). In Schlemm's canal, which drains the aqueous humor of the eye, pressure of the trabecular outflow acting from the basal side of endothelial cells is known to promote the formation of a cavity that eventually segregates into a giant vacuole (Pedrigi et al., 2011). Similarly, in the case of the aortic endothelium, cavity formation suggests the possibility that water accumulation begins in the basal space of HECs, which mechanically bend the plasma membrane. This triggers the invagination of the basal membrane followed by internalization of the cavities into the large vacuoles. Unlike the water-retaining and -secreting roles of the giant vacuoles in Schlemm's canal, vacuoles in the aortic floor eventually show a reduction in their size and disappear from fully rounded HECs (Fig. 1). Consistently, time-lapse imaging analysis revealed that the ectopically induced vacuoles quickly became undetectable before cell detachment (Fig. 4). Elucidation of the regulatory mechanisms underlying rapid vacuole degradation and their significance in HECs will be required to further understand hematopoietic cell emergence. As most Runx1-positive HECs have vacuoles/cavities

at earlier stages (Fig. 1), we expect that vacuole-free HECs are absent or very rare. Whether vacuole-free HECs exist also remains to be analyzed.

The biological significance of water transport for cell floating has been suggested in teleost eggs. Intrinsically, high aqueous-content fish eggs are buoyant in sea water, and this increases the chance of oxygen exchange and dispersal over the ocean (Fabra et al., 2005). We found that endothelial cells that have been water permeated artificially acquire the ability to float in the bloodstream (Fig. 4). Further studies are required to quantitatively determine whether water influx into HECs through AQPs contributes to the buoyancy of hematopoietic cells for circulation and subsequent migration into hematopoietic tissues. The AQP1-overexpressing cells that were released into the bloodstream became CD45-positive cells during circulation (Fig. 4). To date, there is no evidence that non-HEC-derived floating cells convert to hematopoietic cells during circulation. A more-sophisticated avian model for HSC imaging will help to determine whether non-HEC-derived floating cells other than erythrocytes and hematopoietic cells are present during normal development (Davey et al., 2018). In addition, single-cell RNA-seq analysis of these circulating AQP1-overexpressing cells is needed to investigate how endothelial cell properties change after separation from the vascular lumen.

In this study, we performed knockout experiments in quail embryos to elucidate the redundant role of AQPs in EHT. CRISPR/Cas9 genome editing in avian embryos by electroporation is effective for knockout analysis in the normal cell population to circumvent lethal effects; however, technically, it does not destroy all genes in the target cell lineages. To verify that all four AQP genes have loss-of-function mutations in a population with cell rounding defects, it is necessary to perform cloning of AQP genome fragments from these cells residing in the aortic lumen, but it was technically difficult to capture electroporated HECs based on their morphology. Thus, we have not rigorously determined which AQP combinations (or all of them) are most crucial for morphological EHT. In avian embryos, it was challenging to assess the effect of multiple AQP gene knockouts on definitive HSC colony formation in the bone marrow. Further knockout analysis with AQP genes in mouse embryos is needed to elucidate this point. The multilineage potential of multiple AQP-deficient HECs is another issue that needs to be addressed. The *in vitro* stem cell colony formation assay of the aorta, which has been developed for the chick embryo model (Cormier and Dieterlen-Lievre, 1988; Cormier et al., 1986), will help to test the hematopoietic potential of the HECs that failed in morphological EHT.

In summary, this study is the first to demonstrate the involvement of water permeation in EHT using an amniote model system. The findings described here are expected to advance our understanding of embryonic hematopoiesis.

## MATERIALS AND METHODS

### Quail and chicken embryos

Fertilized eggs of tg(pLSi/ $\Delta$ eGFP) chickens (Motono et al., 2010) were obtained from the Avian Bioscience Research Center at Nagoya University. Fertilized wild-type chick eggs were obtained from Fujino Khoka-en (Fukuoka, Japan). Tg(tie1:H2B-eYFP) (Sato et al., 2010) and wild-type quail strains were bred in our own quail breeding facility at Kyushu University. Fertilized eggs were incubated at 38°C until electroporation and subsequent analyses. The staging of quail embryos was based on the Hamburger and Hamilton (HH) stages of chicken embryos (Hamburger and Hamilton, 1951). The animal study was approved by the Institutional Animal Care and Use Committee of Kyushu University (authorization number A20-019).

## Antibodies and immunostaining

Rabbits were immunized four times with an oligopeptide of the C-terminal 252–270 amino acid sequence of quail AQP1 (GenBank XM\_015852703), CEEYDLEGDDMNSRVGMKPK. Antiserum was obtained 56 days after the first immunization (Sigma-Aldrich custom antibody production service). Immunoreactivity against quail AQP1 was confirmed by western blotting (Fig. S2A).

For immunostaining, rabbit anti-AQP1 (1:2000), QH1 (1:500, Developmental Studies Hybridoma Bank) (Pardanaud et al., 1987), rabbit anti-Runx1/AML1+Runx3+Runx2 (1:800, Abcam, ab92336; we specified the immunogen in the aorta as Runx1), mouse anti-Lamp1 (1:1000, Developmental Studies Hybridoma Bank), rabbit anti-LC3B (1:500, Abcam, ab63817), mouse CD45 (1:400, Southern Biotech, NBP1-28295), rabbit anti-cleaved caspase-3 (1:500, Promega, G7481), mouse anti-GFP (1:1000, Abcam, 11814460001), rabbit anti-GFP (1:1000, GeneTex, GTX113617), guinea pig anti-GFP (1:1000, Synaptic Systems, 132004), rabbit anti-mCherry (1:1000, GeneTex, GTX128508), rabbit anti-RFP (1:1000, Invitrogen, R10367), goat anti-RFP (1:1000, Rockland Immunochemicals, 200-101-379), anti-mouse IgG-Alexa Fluor 488 (1:1000, Cell Signaling Technology, 4408), anti-rabbit IgG-Alexa Fluor 488 (1:1000, Cell Signaling Technology, 4412), anti-guinea pig IgG-Alexa Fluor 488 (1:1000, Abcam, ab150185), anti-mouse IgG-Alexa Fluor 594 (1:1000, Cell Signaling Technology, 8890), anti-rabbit IgG-Alexa Fluor 594 (1:1000, Cell Signaling Technology, 8889), anti-goat IgG-Alexa Fluor 594 (1:1000, Abcam, ab150132), anti-mouse IgM-Alexa Fluor 568 (1:1000, Abcam, ab175702), anti-mouse IgG-Alexa Fluor 647 (1:1000, Cell Signaling Technology, 4410) and anti-rabbit IgG-Alexa Fluor 647 (1:1000, Cell Signaling Technology, 4414) were used. Embryos were dissected at the cervical and flank levels in phosphate-buffered saline (PBS) and fixed in 4% paraformaldehyde (PFA)/PBS overnight at 4°C. For CD45 detection (Figs 2F–H and 4F,G,J,K) chick embryos were fixed in 2% PFA/PBS at 4°C for 50 min (E2.5–E3.5) or 80 min (E4–E5). The embryos were embedded in 3% agarose/PBS and sectioned at 140 µm using a vibratome at 5100 mHz (Campden Instruments). The slices were pre-blocked with 5% fetal bovine serum (FBS) and 0.2% bovine serum albumin (BSA)/PBST (0.2% Triton X-100 in PBS) for 1 h at 25°C. They were then incubated overnight at 4°C with a cocktail of primary antibodies diluted with 5% FBS and 0.2% BSA/PBST. After being washed six times in PBST for 30 min at 25°C, the slices were incubated overnight at 4°C with a cocktail of fluorescent secondary antibodies and a fluorescent DNA dye, DRAQ5 (Biostatus), diluted with 5% FBS and 0.2% BSA/PBST. The slices were washed five times in PBST for 30 min at 25°C, transferred into spacers filled with Fluoro-keeper (Nacalai Tesque) on glass slides, mounted with cover glasses and sealed with nail polish. RapiClear 1.47 (SunJin Lab) was used to clear and mount tg(pLSi/DeGFP) chicken-derived specimens. Anti-Runx1 and anti-AQP1 immunostaining were performed sequentially (Fig. 2E). Whole-mount immunostaining and phalloidin staining of E2 embryos (Fig. 4D–G and Fig. S4) and extraembryonic vessels (Fig. 4J,K) were performed as described previously (Sato et al., 2017).

## Post-embedding immunoelectron microscopy

E3.5 (HH20) quail embryos were fixed in 4% PFA and 0.1% glutaraldehyde/PBS. The embryos were then sectioned in the transverse plane at 200 µm using a Linear Slicer PRO10 (Dosaka EM). The preparations were dehydrated using increasing concentrations of methanol, embedded in LR Gold resin (Electron Microscopy Sciences), and polymerized under UV lamps at –20°C for 24 h. Ultrathin sections containing the dorsal aorta (80 nm in thickness) were collected on nickel grids coated with a collodion film, rinsed with PBS several times, then incubated with 2% normal goat serum and 2% BSA in 50 mM Tris (hydroxymethyl)aminomethane-buffered saline (TBS; pH 8.2) for 30 min to block non-specific binding. The sections were then incubated with rabbit anti-AQP1 antibody (1:400, described above) for 1 h at 25°C. To intensify the detectability of the immunoreaction for AQP1, a streptavidin-biotin intensification kit (Nichirei) was used. Sections were first incubated with biotinylated goat anti-rabbit IgG antibody for 10 min at 25°C, followed by incubation with avidin-biotin-horse radish peroxidase (HRP) complex

solution for 5 min at 25°C. The sections were then washed with PBS and incubated with goat antibody against HRP conjugated to 6 nm gold particles (1:50 dilution, Jackson ImmunoResearch Laboratory) for 1 h at 25°C. The sections were contrasted with uranyl acetate and lead citrate, and observed using a H-7650 electron microscope (Hitachi) operated at 80 kV.

## cDNA cloning

Total RNA was isolated from E2 (HH12) quail embryos using NucleoSpin RNA Plus (Macherey-Nagel) and reverse-transcribed using PrimeScript II reverse transcriptase (Takara Bio). Full-length cDNA was amplified using Ex Taq (Takara Bio) or PrimeSTAR GXL DNA polymerase (Takara Bio) with the following primers: XhoI-qAQP1 fw, 5'-CGCTCGAGATGGC-CAGTGAATTCAAA-3' and BamHI-qAQP1 rv, 5'-CAGGATCCTTA-TTTTGGCTTCATTTC-3'; EcoRI-qAQP5 fw, 5'-CCGAATTCATGAAG-AGGGAAATATTA-3' and XbaI-qAQP5 rv, 5'-TATCTAGACTACG-GTGGGGTCAACTC-3'; EcoRI-qAQP8 fw, 5'-TCGAATTCGAGATG-GAGATGGCAGACTC-3' and XbaI-qAQP8 rv, 5'-TGTCTAGATA-CAGCCTCACTTCAGGAAC-3'; XbaI-qAQP9 fw, 5'-TATCTAGAAGC-CAGAATGAGCCGGA-3' and SalI-qAQP9 rv, 5'-GCGTCGACTTACTA-CATGTTCTGTTAGT-3'. The PCR products were cloned into pBluescript II-SK (pBS, Stratagene). Sequences were determined using the ABI 3130 Genetic Analyzer (Applied Biosystems).

## Plasmid vectors

pBS-AQP1-mRFP was generated by inserting the PCR-amplified mRFP derived from pCAGGS-LifeAct-mRFP (Sato et al., 2017) into the 3' end of AQP1 in pBS-AQP1 (described above) using the In-Fusion Cloning system (Takara Bio) with the following primers: qAQP1-mRFP fw, 5'-aagccaaagccaccATGGCCAGCTCCGAGGATGT-3' and mRFP-pBS rv, 5'-gccgtcttagaactTAAAGCGCCTGTGCTATGTC-3' (the sequences for recombination are indicated in lowercase letters). For the construction of AQP1(R196H)-mRFP, pBS-AQP1-mRFP was linearized at BglII and amplified with PCR primers, including the 196th arginine (R) to histidine (H) mutation: qAQP1 R196H fw, 5'-ccagcacatagtttGGCTCAGCACT-GAT-3' and qAQP1 R196H rv, 5'-aaaactatgtctggGTTTATTCCACAG-3'. The PCR product was assembled into a circular plasmid, pBS-AQP1(R196H)-mRFP, by In-Fusion Cloning between 15 bp of the 5' ends (lowercase letters in the primer sequences). pBS-AQP1-2A-eYFP was generated by swapping pBS-AQP1-2A-LifeAct-eYFP and pBS-2A-eYFP at the conserved BamHI and PstI sites. AQP1-mRFP, AQP1(R196H)-mRFP and AQP1-2A-eYFP in pBS were independently subcloned into pCAGGS (Niwa et al., 1991). To construct pCAGGS-H2B-mCherry-2A-AQP1, H2B-mCherry was isolated from pCAGGS-H2B-mCherry by PCR using the following primers (the sequences for recombination are indicated in lowercase letters): pCAG-H2B fw, 5'-atcattttggcaagcttagATGCCAGAG-GCCAGCG-3' and qAQP1-2A rv, gaattcactggccatAGGACCGG-GGTTTTCTTCCA-3', which were inserted into the 5' end of the AQP1 in pCAGGSY-AQP1 by In-Fusion Cloning. To construct pCAGGS-mRFP, mRFP was isolated from pCAGGS-LifeAct-mRFP (Sato et al., 2017) and subcloned into the pCAGGS vector. For the construction of pCAGGS-mRFP-CAAX, the CAAX sequence was isolated from pCAGGS-mCherry-CAAX via PCR using the following primers (the sequences for recombination are indicated in lowercase letters): mRFP-linker fw, 5'-catagcacagggcgtTCCGGACTCAGATCCACGCG-3' and pCAGGS-CAAX rv, 5'-tgattcgacggcgcTCAGGAGAGACACACTTGC-3'. These were inserted into the 3' end of the mRFP in pCAGGS-mRFP by In-Fusion Cloning. pCAGGS-eGFP and pCAGGS-Lyn-mCherry, and have been previously described (Sato et al., 2017). gRNA expression vectors U6.3>gRNA.f+e and U6.3> Control.gRNA.f+e were obtained from Addgene (#99139 and #99140) (Gandhi et al., 2017). Oligo DNAs for the gRNA templates were designed as follows (lowercase letters indicate BsaI overhang): qAQP1 exon2 top, 5'-agatGTCTCCATACAGCTTGCAAA-3' and qAQP1 exon2 bottom, 5'-aaacTTTGCAAGCTGTATGGAGAC-3'; qAQP5 exon1 top, 5'-agatGGCCCACTCCACCATGAAG-3' and qAQP5 exon1 bottom, 5'-aaacCTTCATGGTGGGAGTGGGCC-3'; qAQP8 exon4 top, 5'-aaacGGGCTAACATGTCTGGACCC-3' and qAQP8 exon4 bottom, 5'-aaacGGGCTAACATGTCTGGACCC-3'; qAQP9 exon4 top,



5'-agatGAACAGCTGTTGACATCACC-3' and qAQP9 exon4 bottom, 5'-aaacGGTGATGT- CAACAGCTGTTC-3', qRunx1 exon7 gRNA top, 5'-agatGCCGTCAAGTCAGAAGCACC-3' and qRunx1 exon7 gRNA bottom, 5'-aaacGGTGCTTCTGACTTGACGGC-3'. Annealed oligos were cloned into U6.3> gRNA.f+e according to Stolfi et al. (2014). pCAGGS-Cas9-2A-mRFP was generated by inserting Cas9-2A derived from pCAG-Cas9-2A-Citrin (Addgene plasmid #92358; Williams et al., 2018) into pCAGGS-mRFP by In-Fusion Cloning with the following primers: MCS-nlsCas9 fw, 5'-tcctcgagctagatAACGCTAGGCCACCAT-GGCC-3' and 2A-linker-mRFP rv, 5'-tcggagctggccatGATCTGGGCC-CGGGA-3'. The plasmids were purified using a NucleoBond Xtra Midi EF kit (Macherey-Nagel) and dissolved in TE [10 mM Tris-HCl (pH 8) and 1 mM EDTA].

### Western blot

Cos7 cells at 48 h post transfection of pCAGGS (control) and pCAGGS-AQP1 were suspended with PBS and lysed in same volume of 2× sample buffer (0.125 M Tris-HCl (pH 6.8), 10% 2-mercaptoethanol, sodium 4% dodecyl sulfate (SDS), 10% sucrose and 0.004% Bromophenol Blue) for 3 min at 95°C. Each lysate was separated using SDS-PAGE and blotted using Trans-Blot Turbo (Bio-Rad). The transferred membrane was blocked in 5% ECL Advanced Blocking Agent (GE Healthcare)/PBST (0.1% Tween20/PBS) for 1 h at 25°C, incubated with anti-AQP1 antibody (1:2000, described above) for 1 h at 25°C, washed three times in PBST for 5 min at 25°C and incubated with anti-rabbit IgG-HRP antibody (1:2000, Invitrogen, 656120) for 1 h at 25°C. After washing in PBST three times for 5 min at 25°C, the membrane was immersed in a reaction mix of Western Lightning Plus ECL (Perkin Elmer) and imaged using ImageQuant LAS4000 (GE healthcare).

### In ovo electroporation

For the overexpression experiments, 5 µg/µL of plasmid solution colored with 2% Fast Green FCF (Nacalai Tesque) was prepared. For the CRISPR/Cas9 genome editing, the plasmid solution was mixed as follows: 0.6 µL of U6.3>qAQP1 exon2 gRNA.f+e (5 µg/µL), 0.6 µL of U6.3>qAQP5 exon1 gRNA.f+e (5 µg/µL), 0.6 µL of U6.3>qAQP8 Exon4 gRNA.f+e (5 µg/µL), 0.6 µL of U6.3>qAQP9 Exon4 gRNA.f+e (5 µg/µL), 1.4 µL of pCAGGS-Cas9-2A-mRFP (5 µg/µL) and 2% Fast Green FCF. To transduce the plasmids into the dorsal aortic roof and floor, somite and lateral plate mesoderm progenitors in the primitive streak at E0.75 (HH4-HH5) were targeted. The plasmid solution was injected using a glass capillary and electroporated with a CUY21EX pulse generator (Bex) via the following steps: (1) single poration-pulse at 13 V, 0.08 ms pulse length and 0.05 ms intervals; and (2) three cycles of driving pulses at 6 V, 50 ms pulse length and 50 ms intervals.

### In vitro EHT

Differentiation of the presomitic mesoderm into HECs was performed *in vitro* according to a previous report by Yvernogeu et al. (2016) with slight modifications. Presomitic mesoderm-containing regions were isolated from quail embryos at E2 (HH11-12) using a micro blade K-715 (Feather), followed by brief treatment with Dispase (Wako) in PBS. The presomitic mesoderm was isolated from the surrounding tissues, diced on a silicon-coated Petri dish using tungsten needles and transferred into collagen-coated glass-bottom dishes (Iwaki) filled with a medium (Yvernogeu et al., 2016). The tissues were cultured for 3 days at 37°C in a 5% CO<sub>2</sub> incubator and the medium was replaced each day.

### Fluorescence-activated cell sorting (FACS)

Three days after the start of culture, tissues were dispersed in 0.25% trypsin-EDTA/PBS for 2 min at 37°C, resuspended with culture medium and transferred to 15 ml tubes. After centrifugation and removal of the culture medium, the cells were treated with CellCover (Anacyte Laboratories) for 5 min at 4°C, subsequently incubated with anti-AQP1 polyclonal antibody (1:2000 dilution) and QH1 monoclonal antibody (1:1500 dilution) in CellCover for 30 min at 4°C. After a brief wash in CellCover and centrifugation (180 g, 5 min), the cells were incubated with anti-rabbit IgG

Alexa Fluor 488 (1:1000, Cell Signaling Technology, 4412) and anti-mouse IgG Alexa Fluor 594 (1:1000, Cell Signaling Technology, 8890) in CellCover for 30 min at 4°C. After another brief wash in CellCover and subsequent centrifugation, the cells were resuspended with CellCover to a 1×10<sup>7</sup> cells/ml concentration. AQP1+/QH1+ and AQP1-/QH1- cells were sorted by FACS Aria SORP (Becton Dickinson) and collected into TRIzol LS (Ambion). Total RNA was purified according to the TRIzol LS protocol.

### RNA-seq analysis

After amplification of the cDNA library using the Smart-Seq v4 Ultra Low Input Kit (Clontech), the library was prepared using the NEBNext Ultra RNA library prep kit for Illumina (New England Biolabs). Sequences with 150 bp read length×2 paired ends and 6 GB of data were obtained using the NovaSeq 6000 (Illumina) next-generation sequencer. Sequence products were quality-checked using the software FastQC (Cock et al., 2010), and low-quality sequence ends were removed using Trimmomatic (Bolger et al., 2014). The sequence was then mapped to the Japanese quail reference genome (*Coturnix japonica*, [https://www.ncbi.nlm.nih.gov/assembly/gcf\\_001577835.2](https://www.ncbi.nlm.nih.gov/assembly/gcf_001577835.2)) using HISAT2 (Kim et al., 2015). The number of raw reads mapped to known exon regions was calculated using featureCount (Liao et al., 2014), and then TMP (transcripts per million) values were calculated. The software edgeR (Robinson et al., 2010) was used to calculate the expression variation between samples after normalization using the TMM (trimmed mean of M value) method based on read count values. For gene groups that met the conditions of expression difference log<sub>2</sub> FC (fold change)>1 and *P* value<0.05, MA plots were performed using R to visualize the gene groups with up- and downregulated expression, respectively. GO analyses were performed by Metascape (Zhou et al., 2019) using GO terms for *H. sapiens*.

### Analysis of CRISPR/Cas9 genome editing

Regions with increased expression of mRFP from the three embryos were collected 28 h after electroporation and lysed in 0.15 M NaCl, 10 mM Tris-HCl (pH 8), 10 mM EDTA and 0.1% SDS. Genome fragments of each AQP gene were PCR amplified using MightyAmp DNA polymerase ver.3 (Takara Bio) with the following primers: qAQP1 intron1 fw, 5'-ATGATGGTAGAGGCTGAAC-3' and qAQP1 618 rv, 5'-GTTGTG-TGGCAATCAGTGCTG-3'; qAQP5 exon1-117 fw, 5'-GCTG-CTGTTGCATATATAGA-3' and qAQP5 exon1+272 rv, 5'-CACATA-GAAGAGTGTCCGGA-3'; qAQP8 intron3 fw, 5'-TCACCAGCCTCTG-CAATTAC-3' and qAQP8 intron4 rv, 5'-TATGAAGCCAGCAGA-CATGC-3'; qAQP9 intron 3 fw, 5'-TGTGAAGTGGAGAACTG-3' and qAQP9 intron5 rv, 5'-CAGTACCTAGAGCATGTCTG-3'; BamHI-qRunx1 exon7-166 fw, 5'-atgatccTGCCAGCACTGTGTGTAG-3' and EcoRI-qRunx1 exon7+254 rv, 5'-tcgaattCGAAGGTGAAGTGG-TCTGGA-3' (lowercase letters indicate restriction enzyme sites). The PCR products were cloned into pCR4-TOPO (Invitrogen) or pBS for sequencing. Sequence alignment was performed using the Genetix software (Genetixx).

### Time-lapse microscopy

Electroporated quail embryos were developed *in ovo* until E2 (HH12) and transferred to *ex ovo* as previously described (Sato and Lansford, 2013). Time-lapse imaging of the quail embryos (Fig. 3B,C, Movies 1 and 2) was performed using an upright confocal laser microscope, Fluoview 1200 (Olympus), equipped with a GaAsP detector and thermal stage (Tokai Hit). The embryos were placed in glass-bottomed dishes (Iwaki) coated with agar-albumen media (Chapman et al., 2001) and placed with the glass-bottomed side upwards on the microscopic stage to set the embryos within working distance. Fluorescent signals were imaged using a UPLASPO 30× N.A. 1.05 silicon immersion objective lens with a 235 µm pinhole size, 8 µs/pixel scan speed, 640×640 resolution, 1.80 µm z-intervals and 6-min time intervals. The drifting of the images was corrected using Imaris (Bitplane) as described by Sato and Lansford (2013). For imaging at E3 (Movie 3), electroporated quail embryos were developed *in ovo* until E2 (HH12), transferred to plastic hemispherical cups (40 mm in diameter) with the whole-egg content, and placed inside custom glass-top plastic chambers



humidified with sterilized water. Video rate imaging were performed using an epifluorescence stereomicroscope MVX10 (Olympus) equipped with a custom outer thermal chamber and heating unit SSH300 (Shoei Shokai). Fluorescent signals were imaged using MVPLAPO 2x lens, 3.2× zoom, 512×512 resolution, single plane and stream acquisition was performed using ORCA-Flash 4.0.

### Imaging of immunostained specimens

Immunostained embryo slices and cultured tissues were imaged using Fluoview 1200 through UPLSAPO 30× N.A. 1.05 silicon-, UPLSAPO 60× N.A. 1.30 silicon- and UPLXAPO 100× N.A. 1.47 oil-immersion objective lenses at optimal configurations. For the quantification of apoptotic cells (Fig. S3A,B), whole-mount embryos, immunostained with anti-cleaved caspase-3 antibody, were imaged using a UPLSAPO 10× N.A. 0.40 objective lens at optimal configurations.

### In situ hybridization

Digoxigenin (DIG)-labeled antisense RNA probes for AQP1, AQP5, AQP8 and AQP9 were prepared according to the manufacturer's instructions (Roche). *In situ* hybridization was performed as follows: E3.5 (HH20) quail embryos were fixed in 4% PFA/PBS overnight at 4°C and embedded in paraffin wax. The sections (12 µm) were de-paraffinized twice in xylene for 5 min and rehydrated in a graded ethanol series (twice at 100%, then 90% and 70%; 5 min for each step). After being washed twice with PBST (0.1% Tween 20/PBS) for 5 min, the sections were treated with 2 µg/ml proteinase K/PBST for 7 min at 37°C, followed by refixation in 4% PFA/PBS for 20 min at 25°C. The sections were washed thrice in PBST for 5 min and incubated with 50% formamide, 5× SSC (0.6 M NaCl, 0.06 M tri-sodium citrate dehydrate, pH 5) and 0.5% SDS for 10 min at 25°C. They were then hybridized with the DIG-labeled probes in ULTRAhyb (Invitrogen) overnight at 65°C. The sections were washed in wash solution 1 (50% formamide, 5× SSC and 1% SDS) for 30 min at 65°C, washed twice in wash solution 2 (50% formamide and 2× SSC) for 30 min each at 65°C, and once in a 1:1 mixture of wash solution 2 and TBST [0.8% NaCl, 0.02% KCl, 25 mM Tris-HCl (pH 7.5) and 0.1% Tween 20] for 5 min at 65°C. After washing thrice in TBST for 5 min at 25°C, the sections were pre-blocked with 2% blocking reagent (Roche)/20% FBS/TBST at 25°C for 1 h, followed by incubation with anti-DIG-alkaline phosphatase-Fab fragments (1:1000, Roche, 11093274910) overnight at 4°C. The sections were washed four times for 5 min in 2 mM levamisole/TBST and for 5 min in NTMT [50 mM MgCl<sub>2</sub>, 100 mM NaCl, 100 mM Tris-HCl (pH 9.5) and 0.1% Tween 20]. They were then incubated with 100 µg/ml NBT (Roche) and 37.5 µg/ml BCIP (Roche) in NTMT at 25°C for 6–8 h. After the color reaction, the sections were washed in water for 5 min and dehydrated in a graded ethanol series (50%, 70% and 90% for 5 min at each step, and twice at 100% for 5 min). The sections were immersed in xylene twice for 5 min and sealed with cover glasses using mounting media. Images were captured using a BZ-X700 microscope (Keyence).

### Image segmentation and quantification

The fluorescent signals of Runx1 and DRAQ5 in a constant xyz field size (150.45×150.45×40.00 µm<sup>3</sup>) of the tg(pLSi/ΔeGFP) chick embryo slices were automatically segmented and counted using Imaris (Fig. 1E). Vacuolated cells were manually marked on Imaris, and their numbers were counted (Fig. 1F). To measure cell roundness, optically sectioned eGFP and mRFP images were converted to 8-bit images, threshold levels were adjusted and particle analyses were performed using ImageJ (NIH). Inverted images were used to measure the vacuole area sizes (Fig. 1G,H). Fluorescently inseparable cell clusters and cavities were eliminated from the measurement candidates. In cases where there were multiple vacuoles inside a single cell section, the area sizes were totaled. Runx1-positive HECs were selected for measurement (Fig. 6D–F). Heatmap images of fluorescence intensities of AQP1 and QH1 were generated using ImageJ (Fig. S3C). Nuclear eYFP signals in tg(tie1:H2B-eYFP) embryos were used for the automatic detection and counting of endothelial cells by Imaris (Fig. 6C,G). CD45 and cleaved caspase 3 signals in a constant xyz field size,

1271.2×1271.2×80.5 µm<sup>3</sup>, were automatically detected and counted by Imaris (Fig. 4L; Fig. S4A,B).

### Statistical analyses

The number of analyzed embryos (*n*) is stated in the figure legends. Graph drawing and statistical analyses were performed using GraphPad Prism (GraphPad Software). Unpaired *t*-tests and one-way ANOVA were employed for the comparison of two and multiple groups, respectively. Bars in Figs 1E,F, 3C,D, 4L, 5H,I, 6E,F,K, Figs S4B, S7D,E and horizontal lines in Fig. 1H graphs indicate the mean values.

### Acknowledgements

We thank the Avian Bioscience Research Center at Nagoya University for the provision of transgenic chick eggs and the Research Center for Human Disease Modeling at Kyushu University for the sequencing and FACS support. We also thank, David Huss and Rusty Lansford (Children's Hospital Los Angeles, University of Southern California), Kenji Miyagawa, Xinyi Wang and Takashi Miura (Kyushu University), and Tomohiro Kawahara (Kyushu Institute of Technology) for their help and guidance.

### Competing interests

M.S. is an employee of the Japan Science and Technology Agency. M.S.-K. is an employee of Daiichisankyo RD Novare. The remaining authors declare no competing or financial interests.

### Author contributions

Conceptualization: Y.S.; Validation: Y.S., M.S., M.S.-K., S.M., C.T.; Formal analysis: Y.S., M.S.-K.; Investigation: Y.S.; Resources: Y.S.; Data curation: Y.S., M.S.-K.; Writing - original draft: Y.S.; Visualization: Y.S., S.M.; Supervision: Y.S., H.S.; Project administration: Y.S.; Funding acquisition: Y.S., H.S.

### Funding

This work was supported by the Japan Society for the Promotion of Science KAKENHI (16K14739, 19K06692 and 20H05332 to Y.S. and JP16H06280 to H.S.), by the Kurita Water and Environment Foundation (Y.S.), by the Takeda Science Foundation (Y.S.) and by a Grant-in-Aid for Scientific Research on Innovative Areas Platforms for Advanced Technologies and Research Resources, Advanced Bioimaging Support (ABIS).

### Data availability

RNA-seq datasets have been deposited in the DDBJ Sequenced Read Archive under accession numbers DRX442028 and DRX442029.

### People behind the papers

This article has an associated People behind the papers interview with one of the authors.

### Peer review history

The peer review history is available online at <https://journals.biologists.com/dev/lookup/doi/10.1242/dev.201275.reviewer-comments.pdf>.

### References

- Asai, R., Bressan, M. and Mikawa, T. (2020). Avians as a model system of vascular development. *Methods Mol. Biol.* **2206**, 103–127. doi:10.1007/978-1-0716-0916-3\_9
- Beitz, E., Becker, D., Von Bülow, J., Conrad, C., Fricke, N., Geadkaew, A., Krenc, D., Song, J., Wree, D. and Binghua, W. (2009). In vitro analysis and modification of aquaporin pore selectivity. *Handb. Exp. Pharmacol.* **190**, 77–92. doi:10.1007/978-3-540-79885-9\_4
- Boisset, J. C., Van Cappellen, W., Andrieu-Soler, C., Galjart, N., Dzierzak, E. and Robin, C. (2010). In vivo imaging of haematopoietic cells emerging from the mouse aortic endothelium. *Nature* **464**, 116–120. doi:10.1038/nature08764
- Bolger, A. M., Lohse, M. and Usadel, B. (2014). Trimmomatic: a flexible trimmer for Illumina sequence data. *Bioinformatics* **30**, 2114–2120. doi:10.1093/bioinformatics/btu170
- Bollerot, K., Romero, S., Dunon, D. and Jaffredo, T. (2005). Core binding factor in the early avian embryo: cloning of Cbfb and combinatorial expression patterns with Runx1. *Gene Expr. Patterns* **6**, 29–39. doi:10.1016/j.modgep.2005.05.003
- Bos, F. L., Hawkins, J. S. and Zovein, A. C. (2015). Single-cell resolution of morphological changes in hemogenic endothelium. *Development* **142**, 2719–2724. doi:10.1242/dev.121350
- Bresciani, E., Carrington, B., Yu, K., Kim, E. M., Zhen, T., Guzman, V. S., Broadbridge, E., Bishop, K., Kirby, M., Harper, U. et al. (2021). Redundant

- mechanisms driven independently by RUNX1 and GATA2 for hematopoietic development. *Blood Adv.* **5**, 4949-4962. doi:10.1182/bloodadvances.2020003969
- Champion, L., Linder, M. I. and Kutay, U. (2017). Cellular reorganization during mitotic entry. *Trends Cell Biol.* **27**, 26-41. doi:10.1016/j.tcb.2016.07.004
- Chapman, S. C., Collignon, J., Schoenwolf, G. C. and Lumsden, A. (2001). Improved method for chick whole-embryo culture using a filter paper carrier. *Dev. Dyn.* **220**, 284-289. doi:10.1002/1097-0177(20010301)220:3<284::AID-DVDY1102>3.0.CO;2-5
- Chen, M. J., Yokomizo, T., Zeigler, B. M., Dzierzak, E. and Speck, N. A. (2009). Runx1 is required for the endothelial to haematopoietic cell transition but not thereafter. *Nature* **457**, 887-891. doi:10.1038/nature07619
- Cock, P. J. A., Fields, C. J., Goto, N., Heuer, M. L. and Rice, P. M. (2010). The Sanger FASTQ file format for sequences with quality scores, and the Solexa/Illumina FASTQ variants. *Nucleic Acids Res.* **38**, 1767-1771. doi:10.1093/nar/gkp1137
- Cormier, F. and Dieterlen-Lievre, F. (1988). The wall of the chick embryo aorta harbours M-CFC, G-CFC, GM-CFC and BFU-E. *Development* **102**, 279-285. doi:10.1242/dev.102.2.279
- Cormier, F., De Paz, P. and Dieterlen-Lievre, F. (1986). In vitro detection of cells with monocytic potentiality in the wall of the chick embryo aorta. *Dev. Biol.* **118**, 167-175. doi:10.1016/0012-1606(86)90084-9
- Davey, M. G., Balic, A., Rainger, J., Sang, H. M. and McGrew, M. J. (2018). Illuminating the chicken model through genetic modification. *Int. J. Dev. Biol.* **62**, 85-95. doi:10.1387/ijdb.170315CT
- De Ieso, M. L. and Yool, A. J. (2018). Mechanisms of aquaporin-facilitated cancer invasion and metastasis. *Front. Chem.* **6**, 135. doi:10.3389/fchem.2018.00135
- Dieterlen-Lievre, F. and Martin, C. (1981). Diffuse intraembryonic hemopoiesis in normal and chimeric avian development. *Dev. Biol.* **88**, 180-191. doi:10.1016/0012-1606(81)90228-1
- Dzierzak, E. and Bigas, A. (2018). Blood development: hematopoietic stem cell dependence and independence. *Cell Stem Cell* **22**, 639-651. doi:10.1016/j.stem.2018.04.015
- Eliades, A., Wareing, S., Marinopoulou, E., Fadlullah, M. Z. H., Patel, R., Grabarek, J. B., Plusa, B., Lacaud, G. and Kouskoff, V. (2016). The hemogenic competence of endothelial progenitors is restricted by Runx1 silencing during embryonic development. *Cell Rep.* **15**, 2185-2199. doi:10.1016/j.celrep.2016.05.001
- Fabra, M., Raldúa, D., Power, D. M., Deen, P. M. T. and Cerdà, J. (2005). Marine fish egg hydration is aquaporin-mediated. *Science* **307**, 545. doi:10.1126/science.1106305
- Fellah, J. S., Jaffredo, T., Nagy, N. and Dunon, D. (2013). Development of the avian immune system. In *Avian Immunology* (ed. B. Kaspers and K. Schat), 2nd edn, pp. 45-63. Elsevier
- Gandhi, S., Piacentino, M. L., Vieceli, F. M. and Bronner, M. E. (2017). Optimization of CRISPR/Cas9 genome editing for loss-of-function in the early chick embryo. *Dev. Biol.* **432**, 86-97. doi:10.1016/j.ydbio.2017.08.036
- Garcia, J., Bagwell, J., Njaine, B., Norman, J., Levic, D. S., Wopat, S., Miller, S. E., Liu, X., Locasale, J. W., Stainier, D. Y. R. et al. (2017). Sheath cell invasion and trans-differentiation repair mechanical damage caused by loss of caveolae in the zebrafish notochord. *Curr. Biol.* **27**, 1982-1989.e3. doi:10.1016/j.cub.2017.05.035
- Garcia-Porrero, J. A., Godin, I. E. and Dieterlen-Lievre, F. (1995). Potential intraembryonic hemogenic sites at pre-liver stages in the mouse. *Anat. Embryol.* **192**, 425-435. doi:10.1007/BF00240375
- Gordon-Keylock, S., Sobiesiak, M., Rytsov, S., Moore, K. and Medvinsky, A. (2013). Mouse extraembryonic arterial vessels harbor precursors capable of maturing into definitive HSCs. *Blood* **122**, 2338-2345. doi:10.1182/blood-2012-12-470971
- Hamburger, V. and Hamilton, H. L. (1951). A series of normal stages in the development of the chick embryo. *J. Morphol.* **88**, 49-92. doi:10.1002/jmor.1050880104
- Hancock, J. F., Paterson, H. and Marshall, C. J. (1990). A polybasic domain or palmitoylation is required in addition to the CAAX motif to localize p21ras to the plasma membrane. *Cell* **63**, 133-139. doi:10.1016/0092-8674(90)90294-O
- Howell, E. D., Yzaguirre, A. D., Gao, P., Lis, R., He, B., Lakadamyali, M., Rafii, S., Tan, K. and Speck, N. A. (2021). Efficient hemogenic endothelial cell specification by RUNX1 is dependent on baseline chromatin accessibility of RUNX1-regulated TGF $\beta$  target genes. *Genes Dev.* **35**, 1475-1489. doi:10.1101/gad.348738.121
- Hu, J. and Verkman, A. S., Hu, J. and Verkman, A. S. (2006). Increased migration and metastatic potential of tumor cells expressing aquaporin water channels. *FASEB J.* **20**, 1892-1894. doi:10.1096/fj.06-5930fje
- Hua, Y., Ying, X., Qian, Y., Liu, H., Lan, Y., Xie, A. and Zhu, X. (2019). Physiological and pathological impact of AQP1 knockout in mice. *Biosci. Rep.* **39**, BSR20182303. doi:10.1042/BSR20182303
- Huebert, R. C., Vasdev, M. M., Shergill, U., Das, A., Huang, B. Q., Charlton, M. R., Larusso, N. F. and Shah, V. H. (2010). Aquaporin-1 facilitates angiogenic invasion in the pathological neovasculature that accompanies cirrhosis. *Hepatology* **52**, 238-248. doi:10.1002/hep.23628
- Huo, Z., Lomora, M., Kym, U., Palivan, C., Holland-Cunz, S. G. and Gros, S. J. (2021). AQP1 is up-regulated by hypoxia and leads to increased cell water permeability, motility, and migration in neuroblastoma. *Front. Cell Dev. Biol.* **9**, 605272. doi:10.3389/fcell.2021.605272
- Iizuka, K., Yokomizo, T., Watanabe, N., Tanaka, Y., Osato, M., Takaku, T. and Komatsu, N. (2016). Lack of phenotypal and morphological evidences of endothelial to hematopoietic transition in the murine embryonic head during hematopoietic stem cell emergence. *PLoS One* **11**, e0156427. doi:10.1371/journal.pone.0156427
- Jaffredo, T., Gautier, R., Brajeul, V. and Dieterlen-Lievre, F. (2000). Tracing the progeny of the aortic hemangioblast in the avian embryo. *Dev. Biol.* **224**, 204-214. doi:10.1006/dbio.2000.9799
- Jaffredo, T., Richard, C., Pouget, C., Teillet, M. A., Bollérot, K., Gautier, R. and Drevon, C. (2010). Aortic remodelling during hemogenesis: is the chicken paradigm unique? *Int. J. Dev. Biol.* **54**, 1045-1054. doi:10.1387/ijdb.103062tj
- Kao, Y. C., Jheng, J. R., Pan, H. J., Liao, W. Y., Lee, C. H. and Kuo, P. L. (2017). Elevated hydrostatic pressure enhances the motility and enlarges the size of the lung cancer cells through aquaporin upregulation mediated by caveolin-1 and ERK1/2 signaling. *Oncogene* **36**, 863-874. doi:10.1038/ncr.2016.255
- Khan, L. A., Zhang, H., Abraham, N., Sun, L., Fleming, J. T., Buechner, M., Hall, D. H. and Gobel, V. (2013). Intracellular lumen extension requires ERM-1-dependent apical membrane expansion and AQP-8-mediated flux. *Nat. Cell Biol.* **15**, 143-156. doi:10.1038/ncb2656
- Kim, D., Langmead, B. and Salzberg, S. L. (2015). HISAT: a fast spliced aligner with low memory requirements. *Nat. Methods* **12**, 357-360. doi:10.1038/nmeth.3317
- Kissa, K. and Herbomel, P. (2010). Blood stem cells emerge from aortic endothelium by a novel type of cell transition. *Nature* **464**, 112-115. doi:10.1038/nature08761
- Klaus, A. and Robin, C. (2017). Embryonic hematopoiesis under microscopic observation. *Dev. Biol.* **428**, 318-327. doi:10.1016/j.ydbio.2017.03.008
- Kulesa, P. M., Mckinney, M. C. and McLennan, R. (2013). Developmental imaging: the avian embryo hatches to the challenge. *Birth Defects Res. C Embryo Today* **99**, 121-133. doi:10.1002/bdrc.21036
- Lancino, M., Majello, S., Herbert, S., De Chaumont, F., Tinevez, J. Y., Olivo-Marin, J. C., Herbomel, P. and Schmidt, A. (2018). Anisotropic organization of circumferential actomyosin characterizes hematopoietic stem cells emergence in the zebrafish. *Elife* **7**, e37355. doi:10.7554/eLife.37355
- Li, S. C. and Kane, P. M. (2009). The yeast lysosome-like vacuole: endpoint and crossroads. *Biochim. Biophys. Acta* **1793**, 650-663. doi:10.1016/j.bbamer.2008.08.003
- Liao, Y., Smyth, G. K. and Shi, W. (2014). FeatureCounts: an efficient general purpose program for assigning sequence reads to genomic features. *Bioinformatics* **30**, 923-930. doi:10.1093/bioinformatics/btt656
- Lie-A-Ling, M., Marinopoulou, E., Li, Y., Patel, R., Stefanska, M., Bonifer, C., Miller, C., Kouskoff, V. and Lacaud, G. (2014). RUNX1 positively regulates a cell adhesion and migration program in murine hemogenic endothelium prior to blood emergence. *Blood* **124**, e11-e20. doi:10.1182/blood-2014-04-572958
- Mathai, J. C. and Agre, P. (1999). Hourglass pore-forming domains restrict aquaporin-1 tetramer assembly. *Biochemistry* **38**, 923-928. doi:10.1021/bi9823683
- Maurel, C., Boursiac, Y., Luu, D. T., Santoni, V., Shahzad, Z. and Verdoucq, L. (2015). Aquaporins in plants. *Physiol. Rev.* **95**, 1321-1358. doi:10.1152/physrev.00008.2015
- McLennan, R., Mckinney, M. C., Teddy, J. M., Morrison, J. A., Kasemeier-Kulesa, J. C., Ridenour, D. A., Manthe, C. A., Giniunaite, R., Robinson, M., Baker, R. E. et al. (2020). Neural crest cells bulldoze through the microenvironment using aquaporin 1 to stabilize filopodia. *Development* **147**, dev185231. doi:10.1242/dev.185231
- Meng, F., Rui, Y., Xu, L., Wan, C., Jiang, X. and Li, G. (2014). Aqp1 enhances migration of bone marrow mesenchymal stem cells through regulation of FAK and  $\beta$ -catenin. *Stem Cells Dev.* **23**, 66-75. doi:10.1089/scd.2013.0185
- Morishita, K., Watanabe, K. and Ichijo, H. (2019). Cell volume regulation in cancer cell migration driven by osmotic water flow. *Cancer Sci.* **110**, 2337-2347. doi:10.1111/cas.14079
- Motono, M., Yamada, Y., Hattori, Y., Nakagawa, R., Nishijima, K. and Iijima, S. (2010). Production of transgenic chickens from purified primordial germ cells infected with a lentiviral vector. *J. Biosci. Bioeng.* **109**, 315-321. doi:10.1016/j.jbiosc.2009.10.007
- Nguyen, T., Toussaint, J., Xue, Y., Raval, C., Cancel, L., Russell, S., Shou, Y., Sedes, O., Sun, Y., Yakobov, R. et al. (2015). Aquaporin-1 facilitates pressure-driven water flow across the aortic endothelium. *Am. J. Physiol. Heart Circ. Physiol.* **308**, H1051-H1064. doi:10.1152/ajpheart.00499.2014
- Niwa, H., Yamamura, K. and Miyazaki, J.-I. (1991). Efficient selection for high-expression transfectants with a novel eukaryotic vector. *Gene* **108**, 193-199. doi:10.1016/0378-1119(91)90434-D
- North, T., Gu, T. L., Stacy, T., Wang, Q., Howard, L., Binder, M., Marín-Padilla, M. and Speck, N. A. (1999). Cbfa2 is required for the formation of intra-aortic hematopoietic clusters. *Development* **126**, 2563-2575. doi:10.1242/dev.126.11.2563

- North, T. E., De Bruijn, M. F. T. R., Stacy, T., Talebian, L., Lind, E., Robin, C., Binder, M., Dzierzak, E. and Speck, N. A. (2002). Runx1 expression marks long-term repopulating hematopoietic stem cells in the midgestation mouse embryo. *Immunity* **16**, 661-672. doi:10.1016/S1074-7613(02)00296-0
- Ozu, M., Dorr, R. A., Gutiérrez, F., Politi, M. T. and Toriano, R. (2013). Human AQP1 is a constitutively open channel that closes by a membrane-tension-mediated mechanism. *Biophys. J.* **104**, 85-95. doi:10.1016/j.bpj.2012.11.3818
- Pardanaud, L., Altmann, C., Kitos, P., Dieterlen-Lièvre, F. and Buck, C. A. (1987). Vasculogenesis in the early quail blastodisc as studied with a monoclonal antibody recognizing endothelial cells. *Development* **100**, 339-349. doi:10.1242/dev.100.2.339
- Pardanaud, L., Luton, D., Prigent, M., Bourcheix, L. M., Catala, M. and Dieterlen-Lièvre, F. (1996). Two distinct endothelial lineages in ontogeny, one of them related to hemopoiesis. *Development* **122**, 1363-1371. doi:10.1242/dev.122.5.1363
- Pedrigi, R. M., Simon, D., Reed, A., Stamer, W. D. and Overby, D. R. (2011). A model of giant vacuole dynamics in human Schlemm's canal endothelial cells. *Exp. Eye Res.* **92**, 57-66. doi:10.1016/j.exer.2010.11.003
- Preston, G. M., Carroll, T. P., Guggino, W. B. and Agre, P. (1992). Appearance of water channels in *Xenopus* oocytes expressing red cell CHIP28 protein. *Science* **256**, 385-387. doi:10.1126/science.256.5055.385
- Robinson, M. D., McCarthy, D. J. and Smyth, G. K. (2010). edgeR: a Bioconductor package for differential expression analysis of digital gene expression data. *Bioinformatics* **26**, 139-140. doi:10.1093/bioinformatics/btp616
- Saadoun, S., Papadopoulos, M. C., Hara-Chikuma, M. and Verkman, A. S. (2005). Impairment of angiogenesis and cell migration by targeted aquaporin-1 gene disruption. *Nature* **434**, 786-792. doi:10.1038/nature03460
- Sato, Y. and Lansford, R. (2013). Transgenesis and imaging in birds, and available transgenic reporter lines. *Dev. Growth Differ.* **55**, 406-421. doi:10.1111/dgd.12058
- Sato, Y., Poynter, G., Huss, D., Filla, M. B., Czirok, A., Rongish, B. J., Little, C. D., Fraser, S. E. and Lansford, R. (2010). Dynamic analysis of vascular morphogenesis using transgenic quail embryos. *PLoS One* **5**, e12674. doi:10.1371/journal.pone.0012674
- Sato, Y., Nagatoshi, K., Hamano, A., Imamura, Y., Huss, D., Uchida, S. and Lansford, R. (2017). Basal filopodia and vascular mechanical stress organize fibronectin into pillars bridging the mesoderm-endoderm gap. *Development* **144**, 281-291. doi:10.1242/dev.141259
- Stolfi, A., Gandhi, S., Salek, F. and Christiaen, L. (2014). Tissue-specific genome editing in *Ciona* embryos by CRISPR/Cas9. *Development* **141**, 4115-4120. doi:10.1242/dev.114488
- Teruel, M. N., Blanpied, T. A., Shen, K., Augustine, G. J. and Meyer, T. (1999). A versatile microporation technique for the transfection of cultured CNS neurons. *J. Neurosci. Methods* **93**, 37-48. doi:10.1016/S0165-0270(99)00112-0
- Törnroth-Horsefield, S., Chivasso, C., Strandberg, H., D'agostino, C., O'neale, C. V. T., Schey, K. L. and Delporte, C. (2022). Insight into the mammalian aquaporin interactome. *Int. J. Mol. Sci.* **23**, 9615. doi:10.3390/ijms23179615
- Verkman, A. S. (2002). Aquaporin water channels and endothelial cell function. *J. Anat.* **200**, 617-627. doi:10.1046/j.1469-7580.2002.00058.x
- Wagner, K., Unger, L., Salman, M. M., Kitchen, P., Bill, R. M. and Yool, A. J. (2022). Signaling mechanisms and pharmacological modulators governing diverse aquaporin functions in human health and disease. *Int. J. Mol. Sci.* **23**, 1388. doi:10.3390/ijms23031388
- Wei, X. and Dong, J. (2015). Aquaporin 1 promotes the proliferation and migration of lung cancer cell in vitro. *Oncol. Rep.* **34**, 1440-1448. doi:10.3892/or.2015.4107
- Williams, R. M., Senanayake, U., Artibani, M., Taylor, G., Wells, D., Ahmed, A. A. and Sauka-Spengler, T. (2018). Genome and epigenome engineering CRISPR toolkit for in vivo modulation of cis-regulatory interactions and gene expression in the chicken embryo. *Development* **145**, dev160333. doi:10.1242/dev.160333
- Wu, Y. and Hirschi, K. K. (2021). Regulation of hemogenic endothelial cell development and function. *Annu. Rev. Physiol.* **83**, 17-37. doi:10.1146/annurev-physiol-021119-034352
- Yvernogeu, L. and Robin, C. (2017). Restricted intra-embryonic origin of bona fide hematopoietic stem cells in the chicken. *Development* **144**, 2352-2363. doi:10.1242/dev.151613
- Yvernogeu, L., Gautier, R., Khoury, H., Menegatti, S., Schmidt, M., Gilles, J. F. and Jaffredo, T. (2016). An in vitro model of hemogenic endothelium commitment and hematopoietic production. *Development* **143**, 1302-1312. doi:10.1242/dev.126714
- Zhou, F., Li, X., Wang, W., Zhu, P., Zhou, J., He, W., Ding, M., Xiong, F., Zheng, X., Li, Z. et al. (2016). Tracing haematopoietic stem cell formation at single-cell resolution. *Nature* **533**, 487-492. doi:10.1038/nature17997
- Zhou, Y., Zhou, B., Pache, L., Chang, M., Khodabakhshi, A. H., Tanaseichuk, O., Benner, C. and Chanda, S. K. (2019). Metascape provides a biologist-oriented resource for the analysis of systems-level datasets. *Nat. Commun.* **10**, 1523. doi:10.1038/s41467-019-09234-6



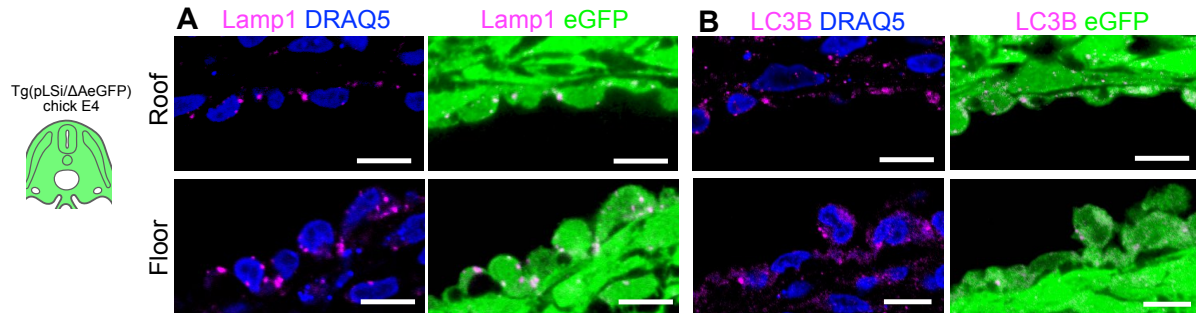


**Fig. S1. Lysosome and autophagosome do not colocalize with the vacuole.**

Optical cross-sections of tg(pLSiΔAeGFP) chick embryos at E4. Lamp1 (A) and LC3B (B) signals were not localized in the eGFP-negative areas. Scale bars: 10  $\mu$ m.

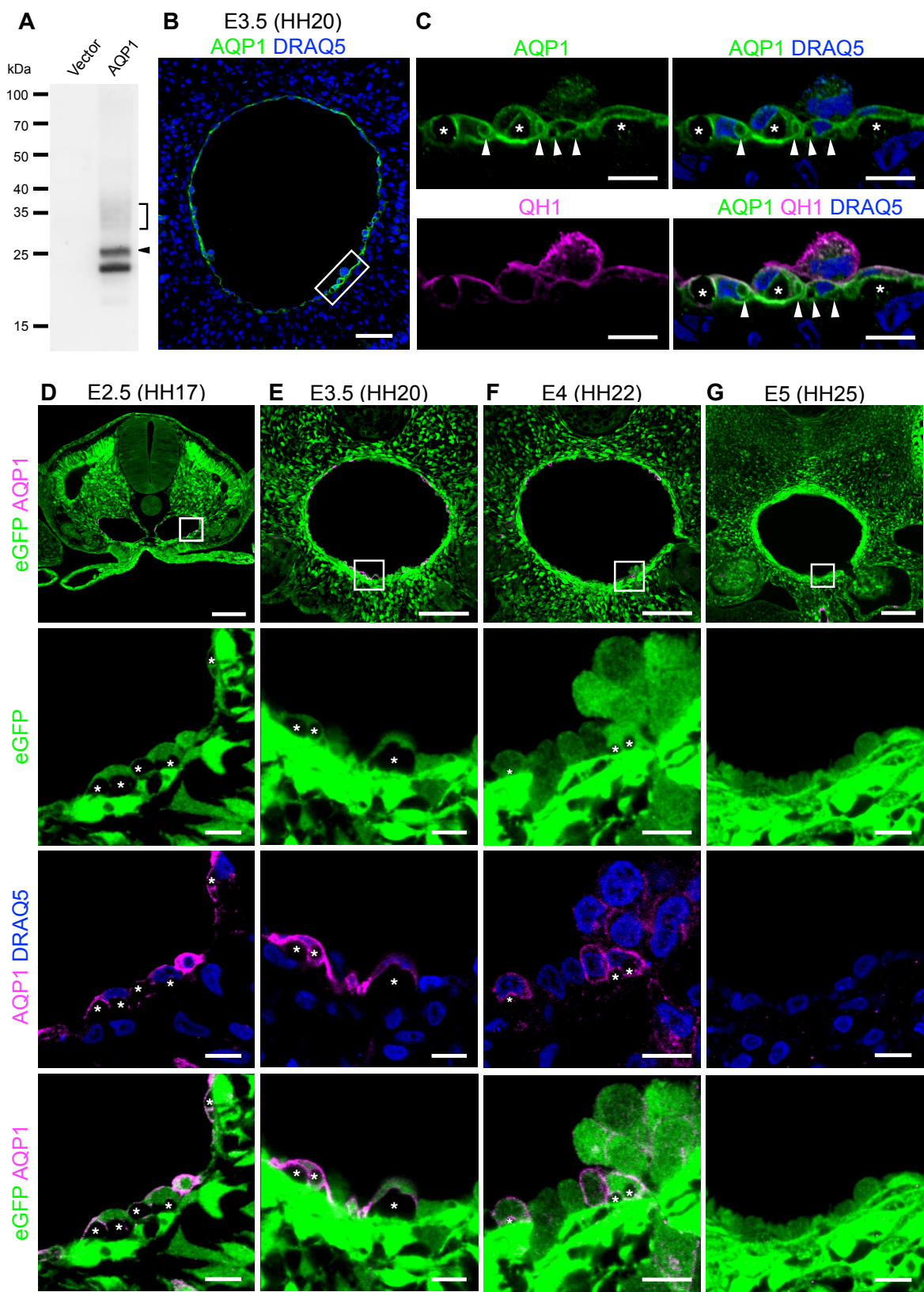


**Fig. S2. AQP1 expression in the aortic endothelial cells diminishes following EHT.**

(A) Western blot of pCAGGS-AQP1 transfected COS lysate using anti-quail AQP1 antibody. 28 kDa AQP1 (arrowhead) and glycosylated AQP1 (bracket) are detected. (B) Optical cross-sections of the aorta in an E3.5 quail embryo. AQP1-expressing cells are distributed in both the roof and floor of the aorta. (C) Magnified view of the rectangular areas in (B). Vacuoles/cavities are indicated by asterisks and arrowheads. AQP1 accumulated in the plasma and vacuolar membranes. The endothelial cell membrane marker QH1 overlapped with AQP1 signals in the plasma membrane. (D–G) Optical cross-sections of tg(pLSiΔAeGFP) chick embryos at E2.5 (D), 3.5 (E), 4 (F), and 5 (G). Squares indicate magnified areas in the lower three panels. AQP1 accumulated in both the plasma and vacuole membranes in the E2.5–4 aortic floor. AQP1 was not expressed in the aorta at E5, concurrent with the disappearance of vacuole/cavity-containing cells (G). Scale bars: 50  $\mu\text{m}$  in (B), 10  $\mu\text{m}$  in (C and lower panels in D–G), and 100  $\mu\text{m}$  in the upper panels in (D–G).



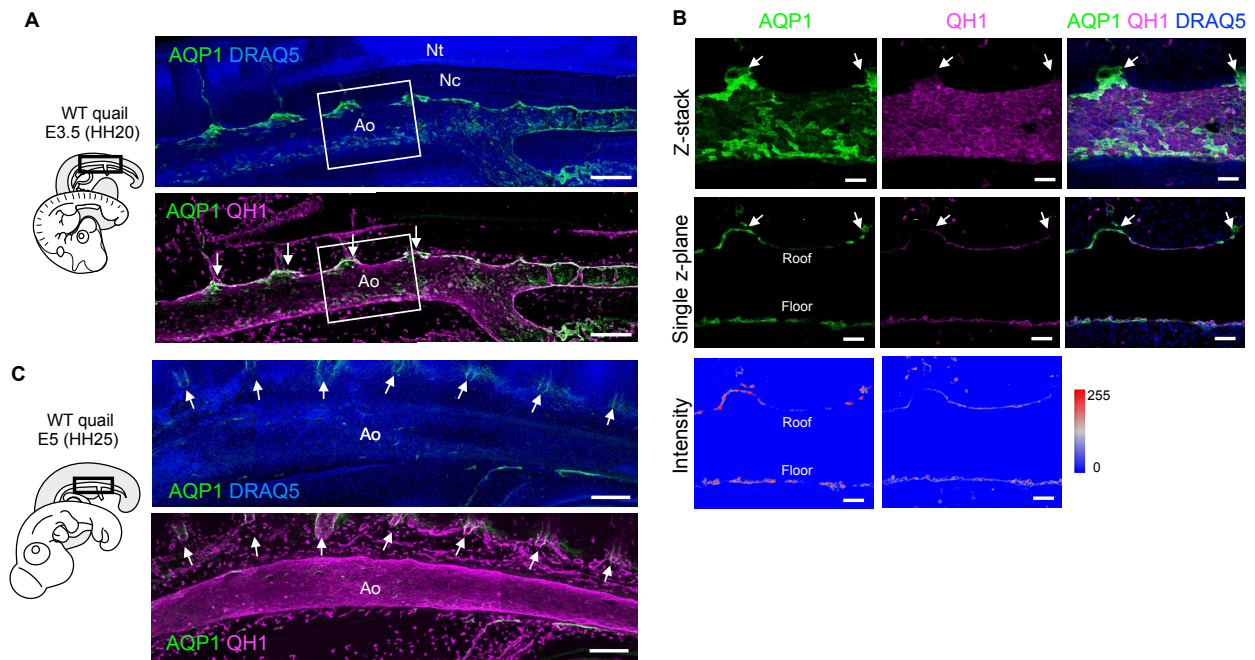


**Fig. S3. AQP1 in the aorta is heterogeneous in distribution pattern and expression level.**

(A and B) Z-stacked images of longitudinal optical sections of WT quail embryos at E3.5 (A) and E5 (B). AQP1<sup>+</sup> cells are not uniformly distributed in the QH1<sup>+</sup> endothelium of the aorta at E4 (A). AQP1<sup>+</sup>/QH1<sup>+</sup> intersegmental vessels (ISVs) are indicated by arrows. Only a few vascular endothelial cells expressing AQP1 are observed in the aorta at E5 (B). In contrast, endothelial cells of the ISVs express AQP1. (C) Magnified view of the rectangular areas in (A). Heat maps of AQP1 and QH1 signal intensities (lower panels) show that AQP1 is highly expressed in the endothelial cells of the aortic floor and part of the aortic roof near the intersegmental vessels (arrows in the upper two panels). Nt: neural tube, Nc: notochord, Ao: aorta. Scale bars: 200  $\mu$ m in (A and B) and 50  $\mu$ m in (C).

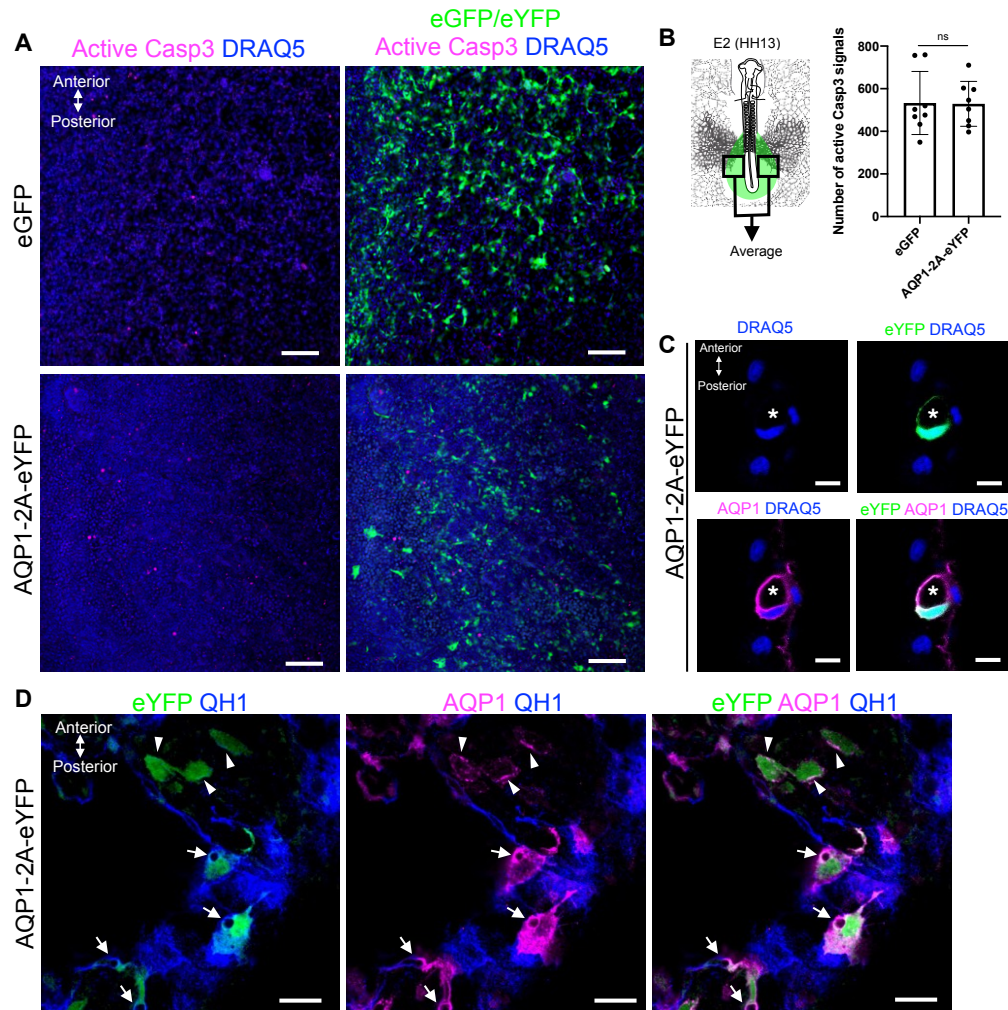


**Fig. S4. Ectopic detachment of AQP1-overexpressing cells is not cell death extrusion.** (A) Z-stacked images of vitelline artery regions in eGFP-(control)- and AQP1-2A-eYFP-overexpressing embryos at E2 (HH13, 28 h after electroporation). Apoptotic cells were detected through active caspase-3. (B) Average number of active caspase-3 signals on the left and right sides per embryo ( $n = 8$ ) is plotted. ns: not significant by unpaired  $t$ -test. (C) Optical horizontal section of the vitelline artery region in an AQP1-2A-eYFP-overexpressing embryo at E2. The DRAQ5 signal represents no apoptotic or necrotic shrinkage/chromatin condensation in the nuclei of AQP1-2A-eYFP-overexpressing cells. The vacuoles are marked with an asterisk. (D) Optical horizontal section of the vitelline artery region in an AQP1-2A-eYFP-overexpressing embryo at E2. AQP1-overexpressing endothelial cells (QH1-positive) with vacuoles are indicated by arrows. Vacuoles were not found in AQP1-overexpressing non-endothelial cells (QH1-negative, arrowheads). ns: not significant, scale bars: 100  $\mu\text{m}$  in (A), 10  $\mu\text{m}$  in (C), and 20  $\mu\text{m}$  in (D).



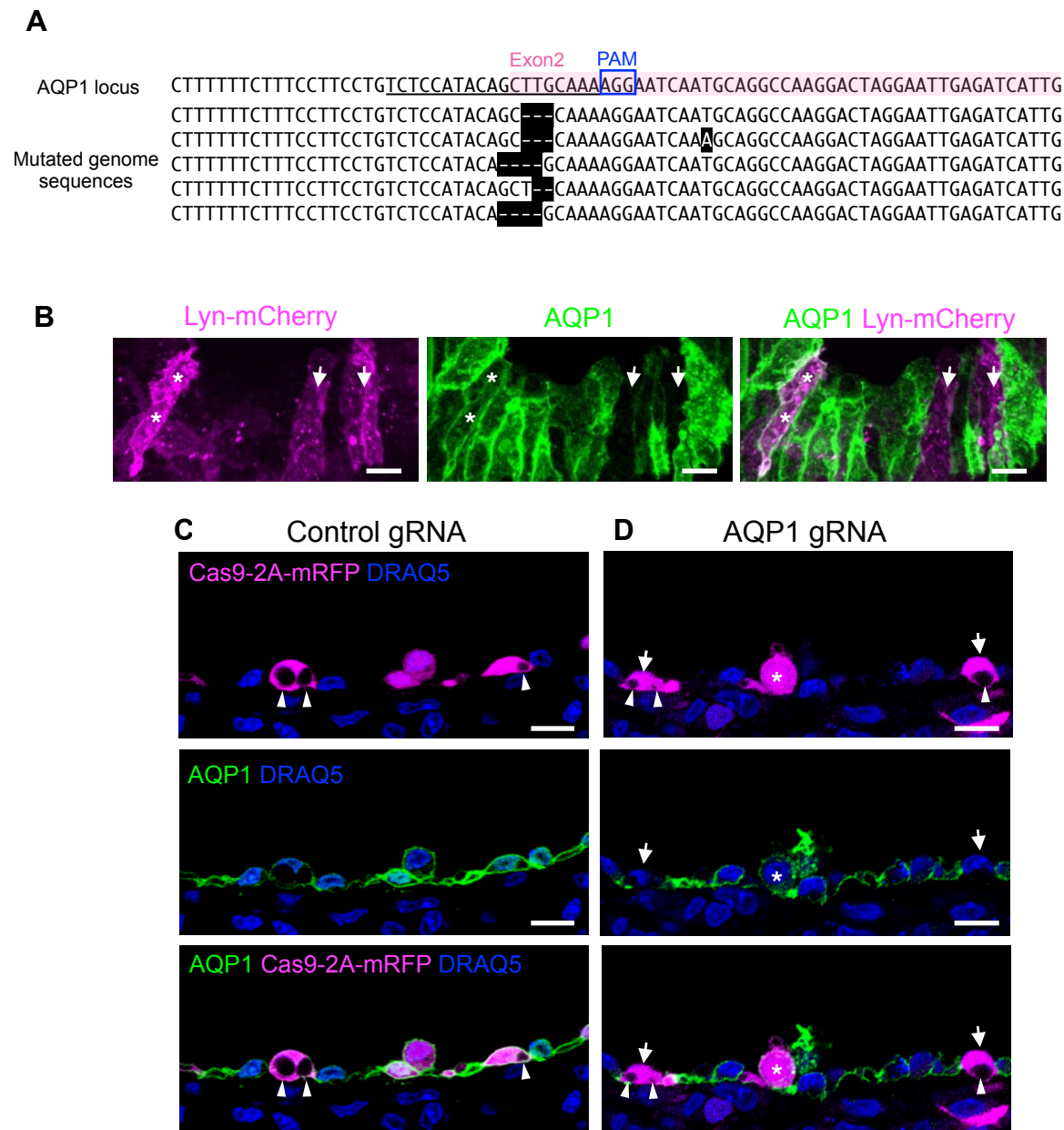


**Fig. S5. *AQP1*-knockout cells become rounded with vacuoles.**

(A) CRISPR/Cas9-mediated mutations in the *AQP1* genome. The guide RNA (gRNA) sequence 77 is underlined. The deletions and mismatches are shaded. Loss-of-function mutations were 78 generated in the target *AQP1* genome locus. (B) Oblique views of Cas9 and *AQP1* gRNA79 -expressed blood vessels in quail embryo at E4. Electroporated cell membranes were labeled with co-electroporated Lyn-mCherry. The *AQP1* protein was not detected in Lyn-mCherry<sup>+</sup> cells

(arrows). AQP1-intact cells were also found in Lyn-mCherry<sup>+</sup> cells (asterisks). These cells are considered to fail in non-homologous end-joining (Williams et al., 2018). (C and D) Optical cross-sections of aortae in control and AQP1 gRNA-electroporated embryos at E4. Electroporated cell bodies and internal vacuoles were identified by mRFP. (C) AQP1 and vacuoles (arrowheads) were not altered in control gRNA-electroporated embryos. (D) Unexpectedly, vacuoles (arrowheads) were observed in AQP1-negative cells (arrows) of AQP1 gRNA/Cas9-2A-mRFP-electroporated embryos (n = 10). AQP1-knockout cells were morphologically indistinguishable from control cells. AQP1-intact/mRFP<sup>+</sup> cells are marked by asterisks. Scale bars: 10  $\mu$ m.



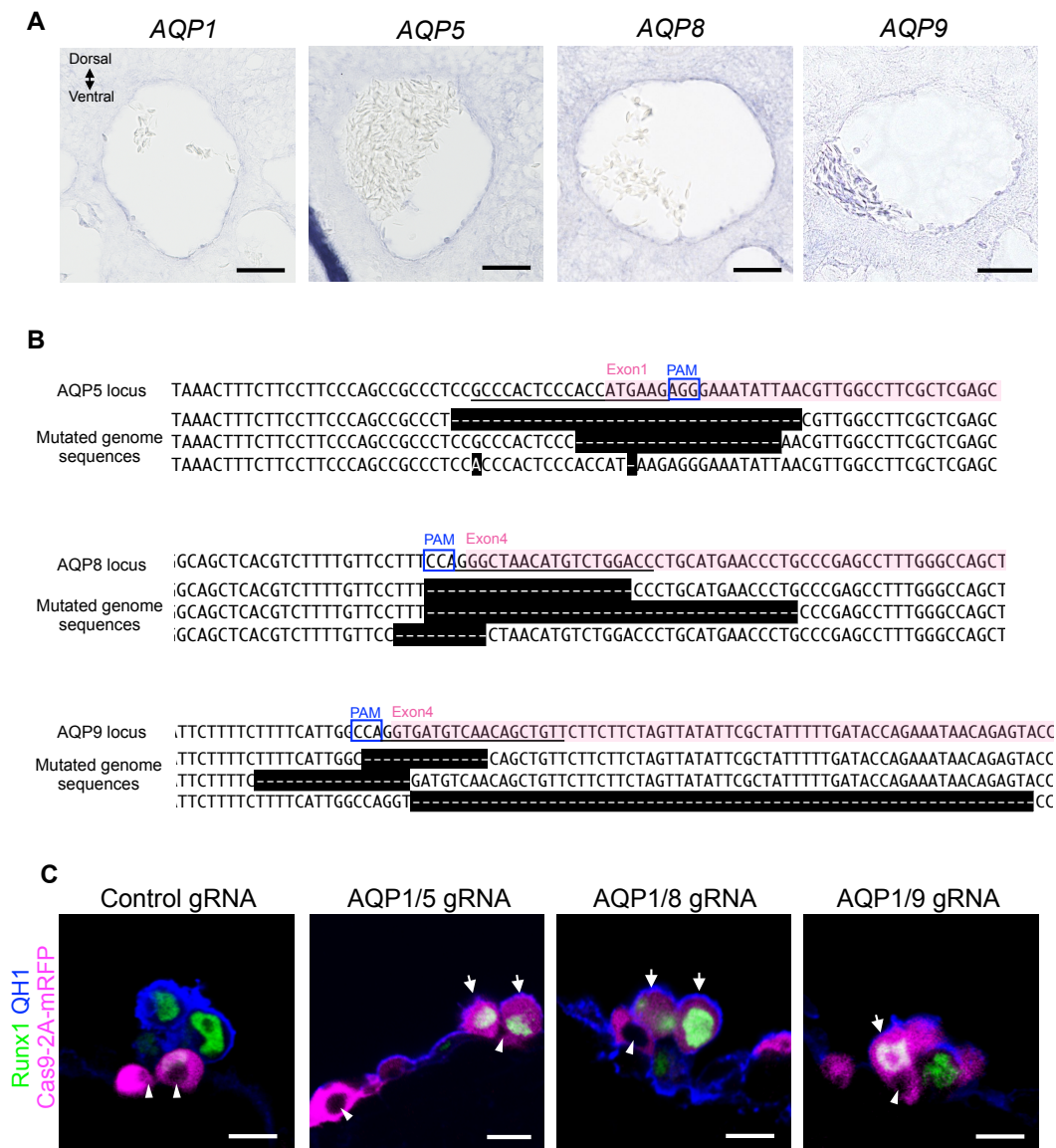


**Fig. S6. AQP1, 5, 8, and 9 are redundantly expressed in the aorta.**

(A) *In situ* hybridization of quail embryos at E3.5. AQP5, 8, and 9 are expressed in the aortic endothelium and surrounding mesenchyme. (B) CRISPR/Cas9-mediated mutations in genes encoding AQP5, 8, and 9. The gRNA sequences are underlined. The deletions and mismatches are shaded. Loss-of-function mutations were generated in the target AQP genome loci. (C) Optical cross-sections of aortae at E4. Electroporated cells and internal vacuoles were identified by mRFP. Vacuoles (arrowheads) were formed in AQP1/5 (n = 5), AQP1/8 (n = 5), and AQP1/9 (n = 6) double-knockout HECs (arrows). Scale bars: 50  $\mu$ m in (A), 10  $\mu$ m in (C).

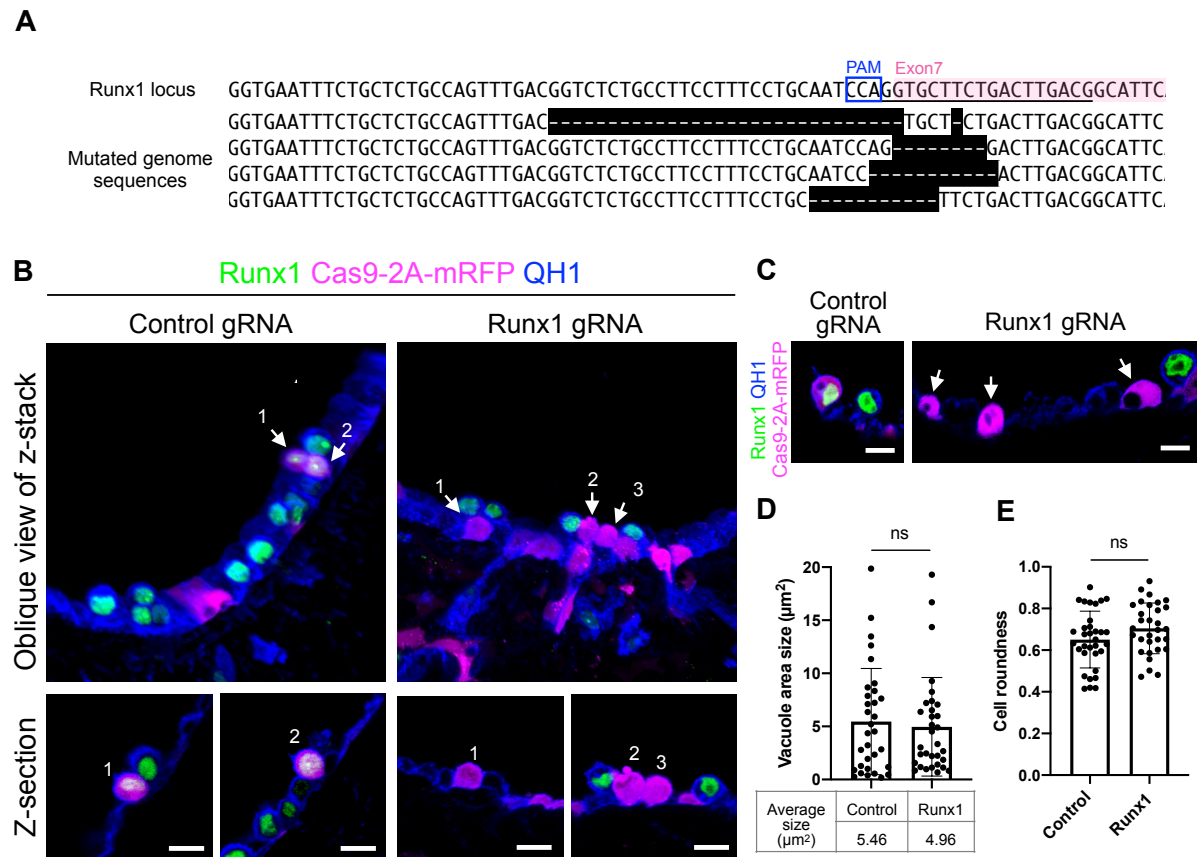


**Fig. S7. Runx1-knockout does not disturb vacuole formation and cell rounding.**

(A) CRISPR/Cas9-mediated mutations in genes encoding Runx1. The gRNA sequences are underlined. The deletions are shaded. Loss-of-function mutations were generated in the target Runx1 genome loci. (B) Oblique views of z-stacked images (upper panels) and optical cross-sections (lower panels) of the aortic floor at E4. Arrows in the left panel: mRFP<sup>+</sup>/Runx1<sup>+</sup> cells in control gRNA-electroporated embryos. Arrows in the right panel: mRFP<sup>+</sup>/Runx1<sup>-</sup> cells in Runx1 gRNA-electroporated embryos. (C) Runx1-knockout cells containing vacuoles are indicated by arrows. (D and E) No statistically significant difference in both vacuole size (D) and cell roundness (H) between control (33 slices, n = 4) and Runx1-knockout cells (31 slices, n = 4). Scale bars: 10  $\mu\text{m}$ .



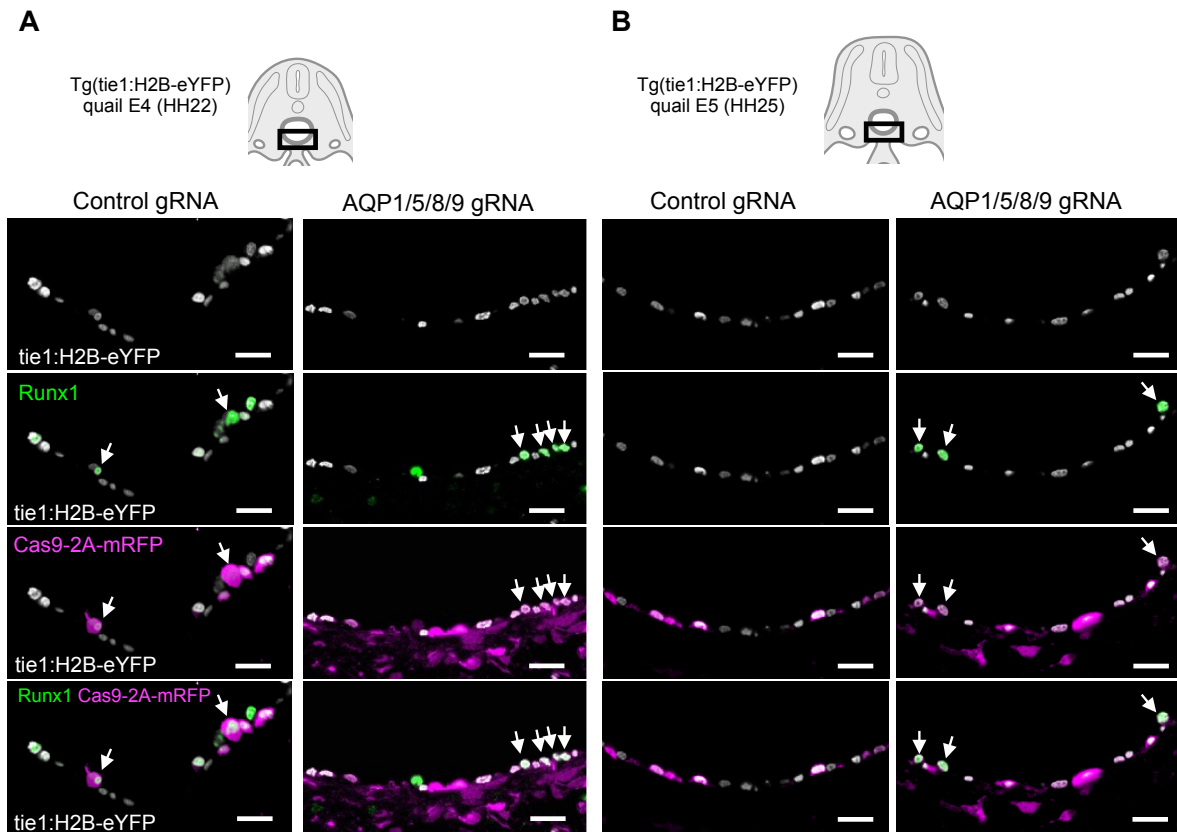
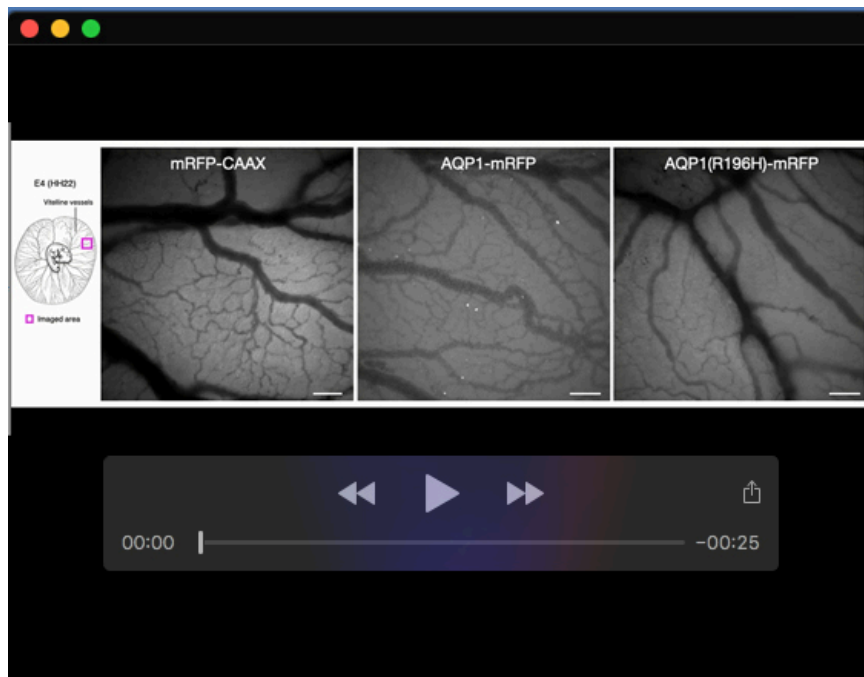
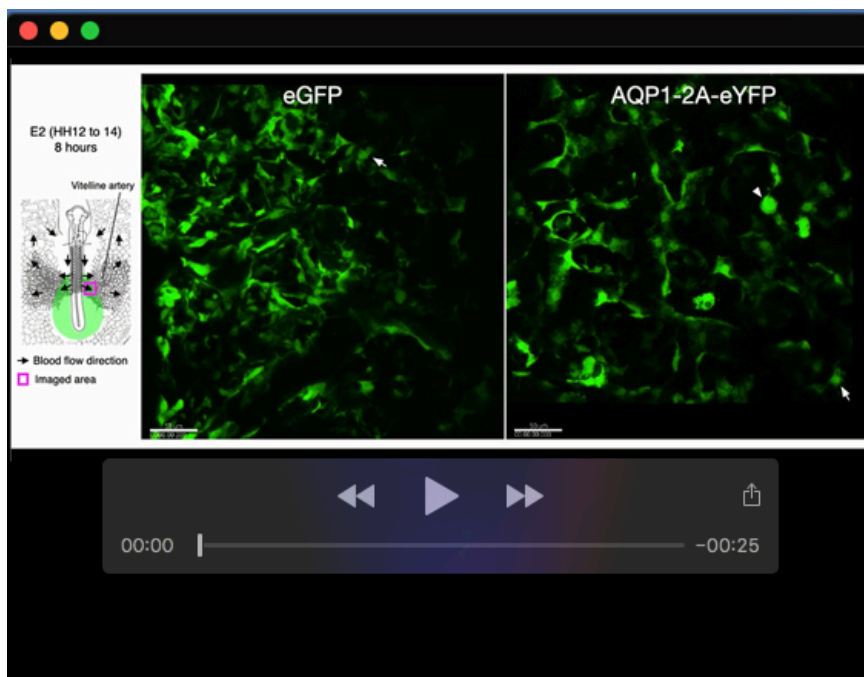


**Fig. S8. Attenuation of AQP family proteins in tg(tie1:H2B-eYFP) embryos.**

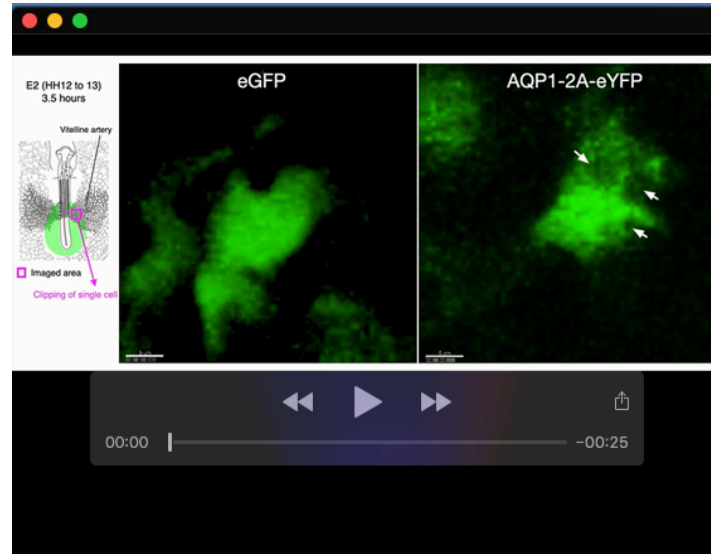
(A and B) Optical cross-sections of aortae in control and AQP1/5/8/9 gRNA-electroporated tg(tie1:H2B-eYFP) embryos at E4 (A) and E5 (B). The mRFP<sup>+</sup>/Runx1<sup>+</sup> cells are indicated by arrows. Endothelial cell nuclei-specific eYFP signals in the tg(tie1:H2B-eYFP) embryo enabled the automatic segmentation and counting of endothelial cells and HECs. Scale bar: 20  $\mu$ m.



**Movie 1. AQP1-overexpressing cells derived from aortic roof are found in circulation.**  
Video rate imaging of vitelline arteries in mRFP-CAAX, AQP1-mRFP, AQP1(R196H)-mRFP-overexpressing embryos at E4. Triple-speed replay. Scale bars: 200  $\mu$ m.

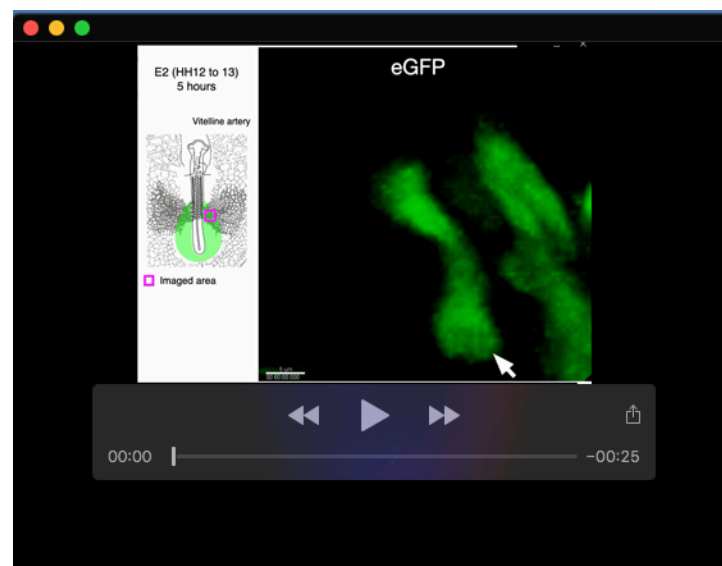


**Movie 2. AQP1-overexpressing cells undergo ectopic cell rounding and detachment.**  
Time-lapse imaging of vitelline vessels in eGFP and AQP1-2A-eYFP-overexpressing embryos at E2. The electroporated region (colored in green), imaged area, and direction of blood flow are illustrated on the left. Freely motile rounded cells are indicated by the arrowheads. The magnified cells in Fig. 4C and Movie 3 are indicated by arrows. Scale bars: 50  $\mu$ m.



### Movie 3. AQP1-overexpressing cells become rounded along with vacuole formation.

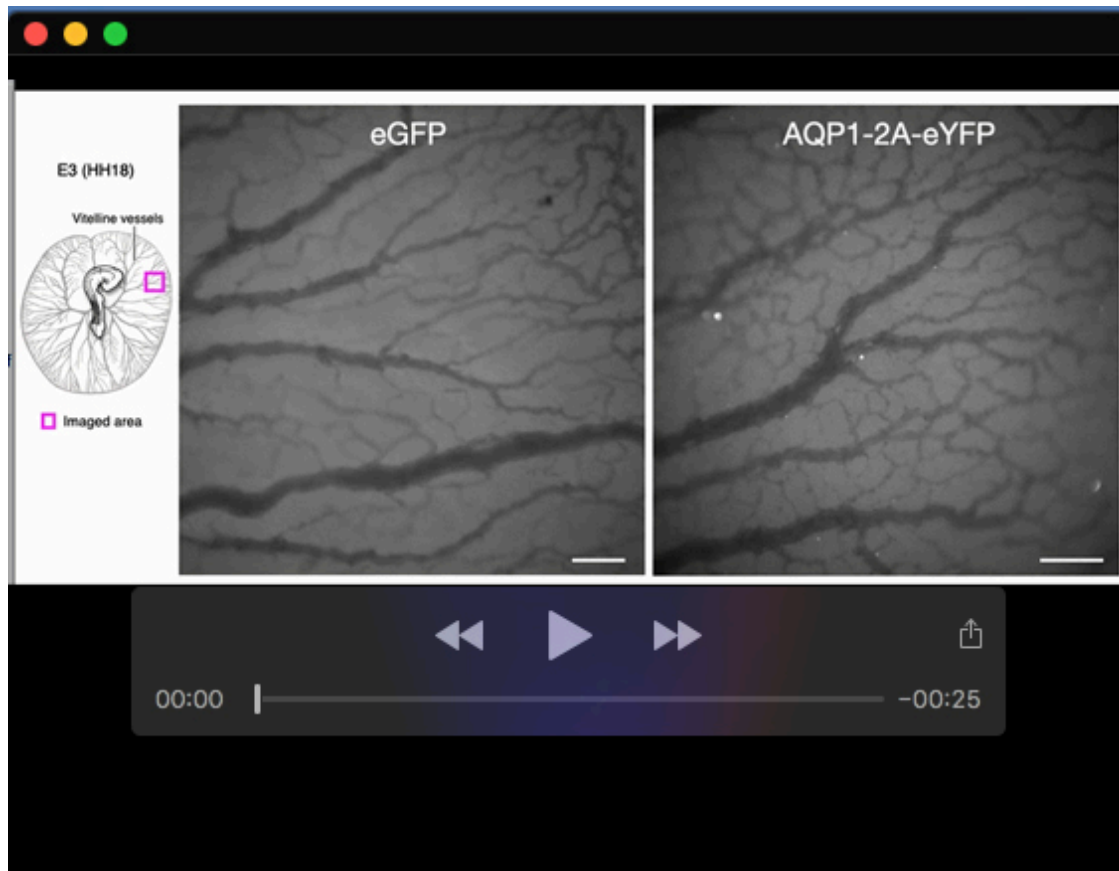
Time-lapse imaging of vitelline vessels in eGFP and AQP1-2A-eYFP-overexpressing embryos at E2. The electroporated region (colored in green) and imaged area are illustrated on the left. Ectopic vacuoles (arrows in the right panel) were formed by AQP1 overexpression, leading to ectopic cell rounding and detachment. Scale bars: 5  $\mu$ m.



### Movie 4. Dividing cell does not form vacuole during mitotic cell rounding.

Time-lapse imaging of vitelline vessels in a control eGFP-overexpressing embryo at E2. Scale bar: 5  $\mu$ m.





**Movie 5. AQP1-overexpressing cells circulate after detachment.**

Video rate imaging of peripheral vitelline arteries in eGFP- and AQP1-2A-eYFP-overexpressing embryos at E3. Triple-speed replay. Scale bars: 200  $\mu\text{m}$ .